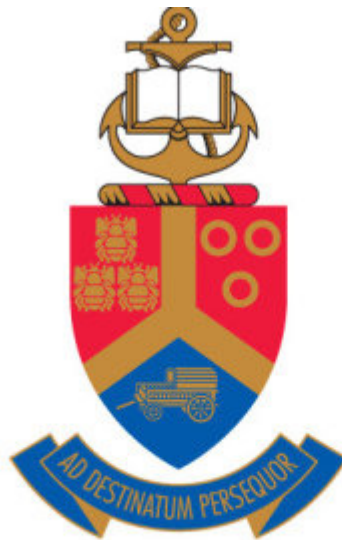# Annealing studies of iodine implanted in pyrolytic carbon

by

Mxolisi Blessing Mukhawana

Submitted in partial fulfilment of the requirements for the degree of

MAGISTER SCIENTIAE

in the Faculty of Natural and Agriculture Sciences at the University of Pretoria

May 2012

Supervisor: Prof. J.B. Malherbe

Co-supervisor: Prof. C.C. Theron

SUMMARY

The behaviour of iodine, before and after annealing, in pyrolytic carbon (PyC) has been studied using the Rutherford backscattering spectrometry (RBS), X-ray diffraction (XRD) and scanning electron microscopy (SEM).

PyC is used as a coating material in the design of the nuclear fuels such as the TRISO particles. TRISO particles are used to produce nuclear energy in nuclear reactors such as the PBMR. Iodine is one of the radioactive fission products produced during the production of nuclear energy by the nuclear fuels. The PyC layers in TRISO particles acts as a barrier for fission products. The main aim of this study was to investigate the effectiveness of PyC as a barrier of iodine diffusion.

360 keV iodine ions were implanted into the PyC to a fluence of 1×10^{15} iodine ions per cm^2, at room temperature. After implantation the PyC samples were annealed (in vacuum) isochronally at 900 °C, 1000 °C, 1100 °C and 1200 °C; all for 9 hours. XRD measurements were performed using a cobalt (Co) XRD spectrometer on θ-2θ configuration; before and after the annealing temperatures. In-lens SEM images were also obtained for the PyC samples before and after heat treatment. RBS measurements were performed using a Van de Graaff accelerator and a 1.6 MeV He^+ beam.

XRD and SEM were used to study the structure of PyC before and after the annealing. Ion implantation and high temperature treatment affected the structure of PyC. Literature has shown that ion implantation caused structural damages in the implanted region of the PyC, reducing the degree of preferred orientation of the graphitic layers of the PyC in that region. The XRD results showed that high temperature annealing caused an increase in the degree of preferred orientation of the graphitic layers in the PyC used which is in agreement with other studies. Comparison of our SEM results to other reports has shown that the PyC used has a structure similar or close to the laminar structures of PyCs, with medium to high degree of preferred orientation.

RBS was used to produce the iodine depth profiles, which provided insight on implantation depth of iodine in PyC as well as iodine behaviour after annealing. The results showed that

iodine concentration in the implanted profile decreased with increasing annealing temperature. The full width at half maximum (FWHM) of the iodine profiles, obtained using the computer program Genplot, showed that after heat treatments of 900 °C, 1000 °C and 1100 °C more iodine initially diffused deeper into the PyC bulk than towards the PyC surface. At 1200 °C, the diffusion of iodine towards the PyC surface increased. It was proposed that this iodine behaviour was associated with the changes in the PyC structure due to ion implantation and high temperature treatment of the PyC. The obtained iodine profiles and the corresponding FWHM did not show evidence that the diffusion of iodine in both directions could be attributed to Fickian diffusion mechanism; hence no activation energy for the iodine diffusion in laminar PyC was determined.

DECLARATION

I, Mxolisi Blessing Mukhawana declare that the dissertation, which I hereby submit for the degree of MSc in Physics at the University of Pretoria is my own work and has not previously been submitted by me for a degree at this or any other tertiary institution.

Signature: ……………………….

Date: ……………………….

TABLE OF CONTENTS

CHAPTER 1:   INTRODUCTION

1.1   BACKGROUND

This study is applicable to safety aspects in the design of modern fuel elements and moderator materials for nuclear reactors. The most common function of nuclear reactors is to produce electricity. Nuclear reactors produce and control nuclear energy, using it in a form of heat to make steam, which in turn is used to drive turbines which produce electricity.

In the heart of a nuclear reactor is the source of the nuclear energy, the nuclear fuel. The nuclear fuel is a material that is used to produce nuclear energy in a controlled and safe manner. The modern high temperature gas-cooled nuclear reactors employ small multilayered fuel spheres either packed in a larger pebble as in the Pebble Bed Modular Reactor (PBMR) or packed in fuel rods stacked in hexagonal graphite blocks. The micro fuel spheres are of UO_2 spheres coated with pyrolytic carbon and silicon carbide layers. These types of fuel particles are called Tri-Structural-Isotropic (TRISO) fuel particles [1-3]. Other types of fuels using PyC as coating materials exist, such as the TRIGA (Training, Research, Isotopes, and General Atomics) fuels, the CANDU fuels, etc.

The TRISO fuel particle consists of a spherical UO_2 fuel kernel which is responsible for the production of nuclear energy by nuclear fission. The UO_2 kernel is surrounded by four layers, first of which is the porous (buffer) pyrolytic carbon (P-PyC) layer, the second is the inner pyrolytic carbon (I-PyC) layer, the third is a silicon carbide (SiC) layer, and lastly the outer pyrolytic carbon (O-PyC); as shown in figure 1-1. All these layers serve as barriers to nuclear fission products. The first layer, the P-PyC, deposited around the kernel is a low density, porous pyrolytic carbon. This is a buffer layer whose function is to absorb recoiling fission products and to provide volume capacity for the gases produced during nuclear fission. This layer deforms easily to accommodate kernel swelling. Another main function is to protect the I-PyC from radiation damage. The second layer, the I-PyC, serves as a barrier to the gaseous fission products, such as iodine (I_2) and protects the SiC layer from chemical attack by oxidizing gases inside the particle. It is a high density and isotropic PyC material. The third layer, the SiC layer serves as the main barrier to fission products. The last layer, the O-PyC, provides mechanical protection to the silicon carbide layer [1-5].

When the uranium (^{235}U) isotope absorbs a slow neutron, it undergoes nuclear fission. The atomic nucleus splits into two or more lighter nuclei, releasing gamma radiation and free neutrons, collectively known as fission products. Fission products are radioactive and may include isotopes of elements ranging from strontium to ruthenium and tellurium to neodymium. They emit alpha, beta and gamma radiation. It was reported that there are approximately 400 fission products (e.g. ^{133}I, ^{90}Sr, ^{134}Cs, ^{109}Ag, ^{95}Zr, ^{144}Ce, etc.) produced by nuclear fission. Most attention is given to radioactive fission products with relatively long half-lives, e.g. strontium, silver, cesium, etc. [4, 6].

Figure 1-1: *Schematic diagram showing the fuel sphere, half section and fuel particle coatings in the fuel element design for PBMR.*

Fission products are mainly released by diffusion from the fuel particle with defects in their coating layers. Diffusion of volatile fission products, such as iodine (^{129}I) with half-lives of six to twenty three years, is important since these nuclides have relatively high mobility in the fuel during normal operation and may be released to the environment during failure of the pyrolytic carbon (PyC) and SiC coatings [6, 7]. Diffusion of volatile fission products out of the TRISO fuel kernel which subsequently leads to their transportation throughout the heat transport system of operating reactors can contribute significantly to occupational radiation exposure.

The success of gas-cooled reactors depends largely upon the safety and quality of the coated fuel particle. In order to carry out reactor safety calculations, it is essential to predict the

escape rate of fission products from the TRISO fuel particles [8]. It is also necessary to produce diffusion coefficient data for the fission products. The above is very useful as it reveals the effectiveness of pyrolytic carbon and the silicon carbide as barriers of fission products in the TRISO particles. The main objective of this study is to determine the effectiveness of the PyC material as a diffusion barrier for iodine. In order to achieve the above, a combination of the following two techniques will be employed; (1) Ion implantation, and (2) Rutherford backscattering spectrometry (RBS).

Iodine will be implanted in pyrolytic carbon specimens and annealed to temperatures up to 1200 °C, or more if necessary. The main advantage of ion implantation is that it provides excellent control of depth and concentration of the introduced impurity, while one of its shortfalls is that it can produce defects which may trap or accelerate the diffusing atom species. RBS will be used to establish concentration–depth profiles for the diffusion of iodine in the pyrolytic carbon and at various temperatures. Diffusion gradients will be determined and used to calculate the corresponding diffusion coefficients [9]. Scanning electron microscopy (SEM) and X-ray diffraction (XRD) will be used as supporting techniques to monitor the microstructures, crystal structure, and isotropy of the pyrolytic carbon before and after annealing.

1.2   LITERATURE REVIEW

There exists a large amount of published work that proves the success of the combination of ion implantation with Rutherford backscattering spectrometry, as tools to study diffusion phenomena in solids. These methods have been applied extensively in studies concerning the diffusion behavior of fission products in the coating layers of fuel particles used in nuclear reactors. However, no published work could be found that provide diffusion data of iodine in pyrolytic carbon, using the combination of ion implantation and Rutherford backscattering spectrometry. Other techniques or approaches produced the following results.

In 1962, Findlay *et al*. [10] produced diffusion results for ^{131}I in graphite using encapsulation or closed tube diffusion method. In their experiment, British pile grade 'A' cylindrical graphite specimens impregnated with uranyl nitrate of natural isotropic composition and fired at 400 °C to convert the nitrate to an oxide (most probably UO_3); were used. To produce fission

products, they were irradiated at about 100 °C in the BEPO (British Experimental Pile 'O') reactor for 6.5 days at a flux of 1.2×10^{12} neutrons cm^{-2}. To remove the uranium, the graphite specimens were leached by successive aliquots of dilute nitric acid. They were then placed inside quartz tubes of 25 cm in length under purified argon at 10 cm Hg pressure, and annealed at 500 °C to 1400 °C; see Figure 1-2. The center section was kept below 50 °C by a jet of compressed air in order to condense released fission products on the walls and thereby maintaining a very low concentration of diffusing vapors at the surface of the graphite.

Figure 1-2:   *Release of non-gaseous fission products; experimental apparatus by Findlay et al.* [10].

The condensates on the walls and the graphite were dissolved using chemicals. These solutions were analyzed for the individual fission product elements using standard radiochemical techniques. Using a suitable model the diffusion coefficient for iodine in graphite was only determined at 800 °C.

A value of $D = 0.17 \times 10^{-20} m^2 s^{-1}$ was reported. It was therefore concluded that the diffusion of iodine in graphite at 800 °C is relatively small. Their investigations on the grain structure of the graphite samples used led to the conclusion that the diffusion therein is a complex process in which migration along crystallite boundaries and passage through small pores is involved in controlling the release of iodine. It was also found that initially, during the first few hours of heat treatment, there was a rapid emission of iodine followed by a slower process whose diffusion coefficient would be a factor of about four lower than the reported one.

Iwamoto *et al.* [9] reported experimental results on the behavior of ^{131}I in graphite after heat treatment. In their experiment, natural graphite powder was used for preparing graphite samples. The graphite samples containing recoiled fission products from uranium were

heated at temperatures ranging between 200 °C and 1450 °C. The heating time ranged from 10 minutes to 24 hours. The heated graphite samples were leached with boiling nitric acid for 1 hour. The graphite powder containing un-leached fission products was separated by filtration from the aqueous leaching solution. The residual graphite obtained was oxidized chemically. An unheated graphite sample was used as a reference sample and was also oxidized. Aliquots of the filtrate and the oxidized graphite solution were measured for the activities of ^{131}I by radiochemical analysis. Concentrations were determined for (1) fission products in the reference sample, (2) those remaining in the residual graphite after nitric acid leaching, and (3) those leached with nitric acid. A suitable method was used to determine the amount of fission products lost from the graphite sample during the heating. Diffusion measurements were not performed.

They concluded that the migration behaviour of iodine in graphite after heat treatment depends on annealing temperature. The amount of migration in the graphite increased with increasing annealing temperature. Their analysis of these results combined with some theoretical considerations of diffusion processes led to them proposing that the iodine escape mechanism from PyC is made up of the following three successive processes; firstly, iodine is released from trapping sites. Secondly, iodine diffuses through the substrate. And thirdly, iodine desorbs from the surface of the substrate. Although they did not measure and calculate the diffusion coefficients for iodine in the graphite, they measured the activation energy for the release process and found it to be 2.0 eV/atom.

In 1970, in their study of the retention of [133]I by pyrolytic carbon-coated nuclear fuel particles, Langer *et al.* [11] prepared pyrolytic carbon-coated thorium-uranium di-carbide microspheres. The kernel (the 200 µm spherical thorium-uranium di-carbide) was coated with a layer of 20-30 µm low density (1.0 g cm^{-3}) buffer pyrolytic carbon followed by a 40-70 µm layer of high density (2.1 g cm^{-3}) isotropic pyrolytic carbon; see Figure 1-3. The two layers of pyrolytic carbon were deposited on the kernel using fluidized bed chemical vapor deposition (FB-CVD).

Some of the particles were irradiated with a fast-flux of 2.7×10^{21} n cm^{-2}. Both the irradiated and un-irradiated particles were leached with hot 13M HNO_3 for 1 hour to remove surface contamination and then activated (short, low level irradiations) at ambient temperature in the

TRIGA reactor to produce inventories of the ^{133}I fission product. The samples were then annealed at 1100 °C and 1300 °C using a graphite tube furnace.
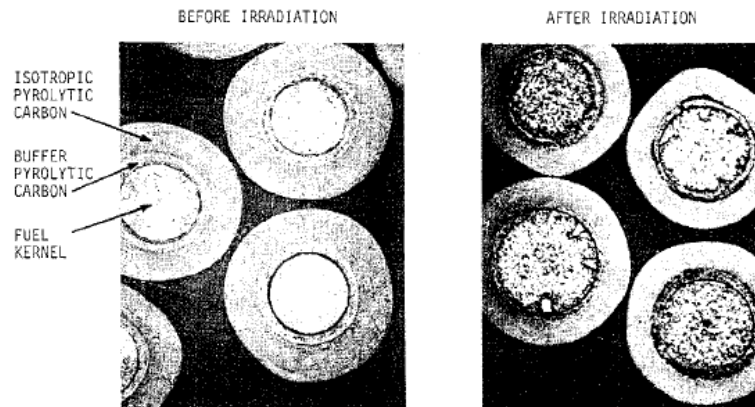

Figure 1-3:   *Photomicrographs of typical BISO fuel particles before and after irradiation (60×) produced by Langer et al* showing the two layer PyC structure.

During annealing, the released ^{133}I was collected and analyzed by determining its fractional release from the isotropic PyC as a function of time and temperature.

Their results showed that the retention of ^{133}I by the irradiated particles that were annealed at 1100 °C was 94% and ^{133}I retention by those annealed at 1300 °C was 95%. Since release from intact particles at ambient temperatures, both during and after the irradiation, does not occur, these percentage values are equivalent to 100% retention within the uncertainty of the measurements. They concluded that the release of iodine is unaffected by irradiation, so both irradiated and non-irradiated would produce similar results. Using other literature, they proposed that the release of iodine fission product from pyrolytic carbon-coated fuel particles are controlled by diffusion of these nuclides through grain boundaries, cracks, and defects in the isotropic pyrolytic carbon coating. When coatings are intact, however, the release of iodine is low. They concluded that isotropic carbon provides excellent retention of iodine.

In 1983, Silverstroni *et al.* [12] studied the transfer of iodine through graphite in aqueous iodide solutions. Their experimental set up consisted mainly of poly-crystalline graphite diaphragms separating two solutions of aqueous KI as well as a mixture of NaI and $HClO_4$ The solutions contained different amounts of I_2. The transfer of iodine from the more concentrated to the more diluted side of the graphite diaphragm was accomplished by electrochemical reduction of I_3^- to I^- on the side facing the concentrated solution and simultaneous oxidation of I^- to

I_3^- on the other side. Using suitable methods described in the paper, they calculated the I_2 concentration in the two solutions of the cell.

The authors found that iodine transfer from the concentrated to the dilute solution occurred through the graphite diaphragm for all the I_2 concentrations and the type of solutions used. They concluded that if the I_2 transfer would be of diffusive nature, the rate of transfer of iodine (dn/dt) should be proportional to the iodine concentration difference $\Delta C = [I_2]_{conc} - [I_2]_{dil}$ according to $\left(\dfrac{dn}{dt}\right)_t = D(\Delta C)_t\left(\dfrac{s}{t}\right)$; wherein S represents the area of the graphite diaphragm, l represents the diaphragm thickness and D represents the diffusion coefficient of the iodine in the graphite. The obtained diffusion rates for iodine were all plotted against time but the diffusion coefficients were not reported. From their diffusion results and iodine transfer rates results, they were able to conclude that if two solutions, both containing the oxidized and the reduced form of the same chemical species in two different concentrations, are separated by a porous diaphragm with metallic conductivity, their mixing is much faster than the purely diffusive nature.

The above literature survey shows that much attention has already been given on the study of the behaviour or diffusion of iodine in Carbon materials. A variety of results have been reported on the diffusivity of iodine in carbon materials. However, the literature did not report on the structure of the carbon materials used and how the structure influences the diffusion of iodine. For instance Findley *et al.* and Iwamoto *et al*. used compressed powder graphite samples. These studies did not put emphasis on how the structure of their carbon materials and their sample preparation methods affects the diffusion of iodine. Another example is that Langer *et al*. did not report the effect of neutron irradiation on the structure of the isotropic PyC used and how it affected the iodine diffusion; if it does at all. Since it is anticipated that the structure of the PyC substrate will affect the behaviour or diffusion of iodine, our study will employ the use of SEM and XRD to monitor the PyC structure after implantation and high temperature annealing. Based on the above and the fact that different sample preparation methods have been employed, we anticipate that our results may differ to a certain extent from what is reported in literature.   As will be reiterated again in section 1.3, none of the papers in our literature search on the behaviour / diffusion of iodine in the carbon materials, employed the combination of RBS and ion implantation. The techniques used in

these studies (leaching, closed tube, etc.) seem to be complex compared to what will be used in this study.

Studies and experimental work has been done in the 1960's and 1970's on the characterisation of pyrolytic carbon using both X-ray diffraction and scanning electron microscopy. More recently, most of the work done has been specifically for nuclear reactor applications. In 2007, Hélary *et al.* [13] used SEM and XRD to characterize the microstructures of both the buffer PyC and the I-PyC. Their main objective was to recover the 1970's analytical expertise by J.C. Bokros and others and compare the results found by those in recent work. Their characterization results proved to be consistent with the results produced by Bokros *et al.* [14, 15]. These studies have shown that the microstructures, crystal structures, density and isotropy / anisotropy of pyrolytic carbon depend on the deposition conditions, and are affected by high-temperature treatment. Changes in microstructures, crystal structure, and isotropy may subsequently affect the diffusion behaviour of foreign atoms (fission products) in pyrolytic carbons [16, 17].

1.3   PROBLEM STATEMENT AND PROJECT SCOPE

None of the papers in our literature search on the behaviour of iodine in PyC used the combination of RBS and ion implantation. The techniques used in these studies (leaching, closed tube, etc.) seem to be complex, involving the use of dangerous chemicals and are relatively difficult to perform. Besides these perceived disadvantages, it is important that as many as possible techniques are utilized and compared against each other in order to give good credibility to the obtained results. This study aims to add another dimension to the study of iodine in PyC by using the combination of RBS and ion implantation. Studies performed during the 1960's and more recently in 2007 showed that the structure of PyC is very much influenced by high temperature treatment. It is expected that this will have a significant influence on the diffusion of iodine in PyC. Hence in addition to RBS, XRD and SEM were also employed.

Polished PyC samples, purchased from SPI supplies were implanted with iodine at the University of Jena, Germany. The samples were then cut into proper sizes and their surfaces

carefully analyzed using the Zeiss Ultra Plus 55 FEG SEM (field emission gun scanning electron microscopy) at the Laboratory for Microscopy and Microanalysis at the University of Pretoria. The implanted samples were then annealed in vacuum and at temperatures ranging from 900 °C to 1200 °C using the WEBB 77 oven (RD Webb Company) at the Physics Department of the University of Pretoria. These temperatures were chosen because the PBMR reactor operates at around 750 to 1000 °C. After annealing, the samples were again analyzed using SEM. Rutherford backscattering spectrometry (RBS) of the University of Pretoria was used to determine the depth profiles and movement of iodine in PyC before and after heat treatment. SEM and XRD were used to characterize the topography and the microstructure of the PyC before and after each annealing step.

The iodine peak shapes obtained from RBS before and after heat treatment were analyzed using a non-linear least square fit method for the purpose of determining their full width at half maximum (FWHM). This was achieved using no-linear least square fit methods (Gaussian and / or Edgewoth). In cases where the FWHM revealed Fickian diffusion to have taken place, the activation energy was estimated. In cases where iodine release could not be attributed to Fickian diffusion, an escape model was proposed. The conditions used in ion implantation, RBS, heat treatment, SEM, and XRD are discussed in chapter 5 and the results in chapter 6.

1.4   REFERENCES

[1]   E. Lopez-Honorato, P.J. Meadows, R.A. Shatwell, and P. Xiao. Carbon **48** (2010) 881-890.

[2]   J.B. Malherbe, E. Friedland and N.G. van der Berg. Nucl. Instr. Meth. **B266** (2008) 1373.

[3]   N.G. van der Berg, J.B. Malherbe, A.J. Botha, E. Friedland and WA Jesser, Surf. Interface Anal. **42** (2009) 1156.

[4]   P.E. Brown and R.L. Faircloth. J. Nucl. Mater. **59** (1976) 29 – 41.

[5]   O.O. Gülol, U. Colak and B. Yildirim. J. Nucl. Mater. **374**, (2006), 168-177.

[6]   http://en.wikipedia.org/wiki/Pebble_bed_reactor. 10 March 2010.

[7]   K. Sawa, S. Shiozawa, K. Fukuda and Y. Chihashi. J. Nucl. Sci. Technol. **29** (1992) 842-850.

[8]   G. K. Miller, D. A. Petti, D. J. Varacalle, and J. T. Maki. J. Nucl. Mater. **295** (2001) 205 – 212.

[9]   K. Iwamoto and J. Oishi. J. Nucl. Mater. **29** (1969) 285 – 301.

[10]   J.R. Findlay, T.F. Laing. J. Nucl. Mater. **7** (1962) 182 - 191.

[11]   S. Langer, C.C. Adams, E.E. Anderson, J.N. Graves and T. Yamaguchi. Adv. Chem. **93** (1968) 63-70.

[12]   P. Silvestroni and F. Rallo. Electrochemica Acta. **12** (1983) 1793 - 1797

[13]   D. He´lary, B.O. Dugne and X. Bourrat. J. Nucl. Mater. **373** (2008) 150–156.

[14]   J.C. Bokros and R.J. Price. Carbon **3** (1966) 503 – 519.

[15]   P.L. Walker. Chemistry and Physics of carbon, A series of advances. **5** Marcel Dekker, Inc, New York (1969).

[16]   E. López-Honorato, P.J. Meadows, P. Xiao, G. Marsh, and T.J. Abram. Nucl. Eng. and Design. **238** (2008) 3121–3128.

[17]   J.D. Hunn, G.E. Jellison and R.A. Lowden. J. Nucl. Mater. **374** (2008) 445-452.

CHAPTER 2:   DIFFUSION IN SOLIDS

2.1   DIFUSSION MECHANISMS

Diffusion is the process by which matter is transported from one part of a system to another as a result of random molecular motions and chemical potential differences in the system. Diffusion in crystals can take place by several distinct atomic processes, depending on crystal imperfections such as point defects (vacancies or impurity atoms) and line or plane defects (dislocations or stacking orders). Some of the most common atomic diffusion mechanisms are briefly discussed below;

2.1.1   Vacancy mechanism

All crystals, including Pyrolytic carbon, in thermal equilibrium above absolute zero, have some unoccupied lattice sites (vacancies). An atom can jump from its lattice position into a neighboring vacancy; as shown in figure 2-1(a). In this case, each diffusing atom moves through the crystal by making a series of exchanges with vacancies which appear adjacent to it from time to time [1, 2].
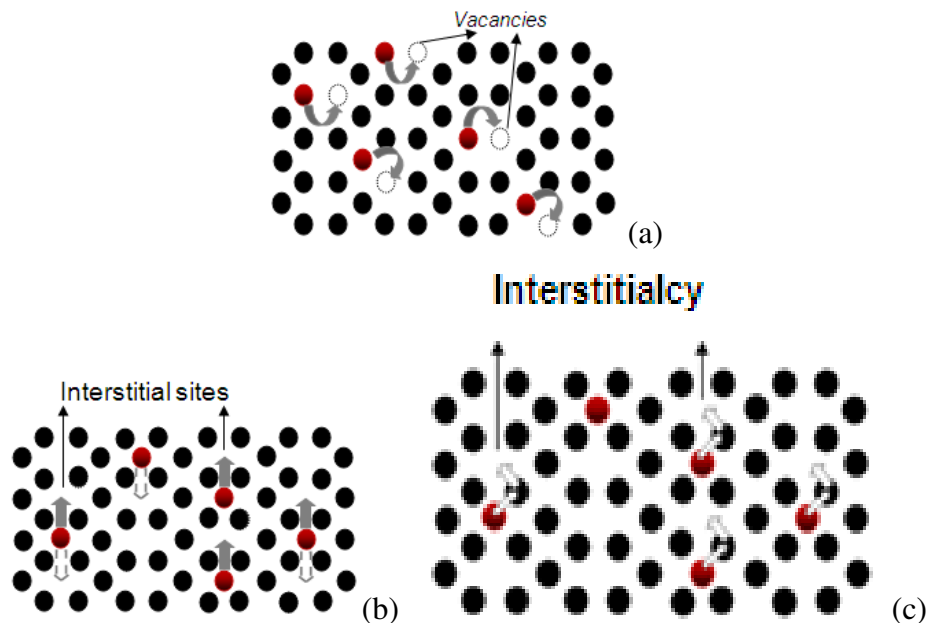

Figure 2-1:   *(a) Vacancy mechanism, (b) Interstitial mechanism, and (c) Interstitialcy mechanism.*

2.1.2   Interstitial mechanism

In this process, atoms that occupy interstitial positions in the lattice move through the crystal by jumping directly into the neighboring interstitial sites; as shown in figure 2-1(b). The energy required for such a jump is much smaller that required in the vacancy mechanisms discussed above [1, 2].

2.1.3   Interstitialcy mechanism

When diffusing interstitial atoms have sizes comparable to that the lattice atoms, the interstitial atoms move into normal lattice sites by pushing neighboring lattice atoms into adjacent interstitial sites; as shown in figure 2-1(c) [1, 2].

2.1.4   Interchange mechanism

In this diffusion mechanism, two or more neighboring lattice atoms interchange their positions in the lattice by rotating about a common center; as shown in figure 2-2(a). An excessively large amount of energy is required for this mechanism and hence believed to be most unlikely to take place [1, 2].

(a)   (b)

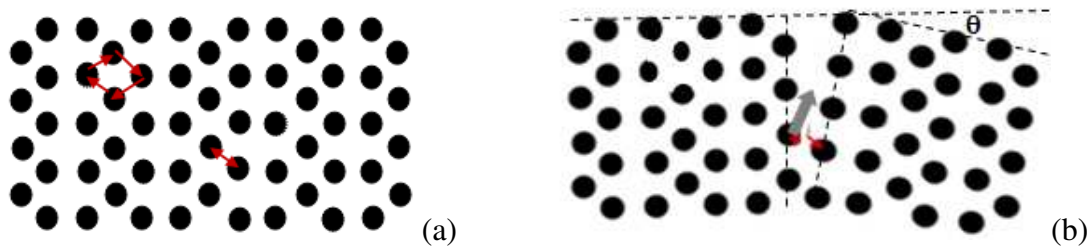**Figure 2-2:**   (a) Interchange mechanism and (b) Sub-boundary mechanism.

2.1.5   Sub-boundary mechanism

The diffusing atom moves along interconnecting dislocation pipes, which results from naturally occurring low angle boundaries; as shown in figure 2-2(b). This mechanism has been found to operate at low temperatures, typically less than $0.5T_m$, where T_m is the absolute melting temperature, in metals [1, 2].

2.1.6   Relaxion mechanism

This mechanism is based on the assumption that diffusing atoms move more or less freely within a disordered group of atoms within the lattice. It has been ruled out in most crystalline solids but has been considered in recent years in the context of radiation damage in amorphous metallic alloys and some polymers [1, 2].

Walker [3] reported that the diffusion paths through carbon deposits are almost exclusively along crystal defects such as crystalline and cone boundaries and that the diffusivity of foreign atoms in pyrolytic carbon (except Boron which can take substitution lattice positions are most likely reduced by high temperature annealing treatment because this annealing reduces many crystal defects.

2.2   MATHEMATICAL MODEL FOR THE DIFFUSION OF FOREIGN ATOMS IN SOLIDS

The mathematical model for diffusion in an isotropic substance is based on the hypothesis that the transfer rate of diffusing substance through a unit area of a section is proportional to the concentration gradient measured normal to the section, i.e.

$$F = -D\frac{\partial C}{\partial x} \qquad (2\text{-}1)$$

In equation 2-1, F is the flux across a given section (the rate of transfer per unit area), C is the concentration of diffusing substance (iodine), D is the diffusion coefficient, and x is the space-coordinate measured normal to the section. Equation 2-1 is called Fick's first law of diffusion. In order to derive a diffusion solution for this study, Fick's second law of diffusion must be used [4]. Consider a rectangular bar of unit cross-sectional area, with the x-axis through the center. The dimensions thereof are given in Figure 2-3.
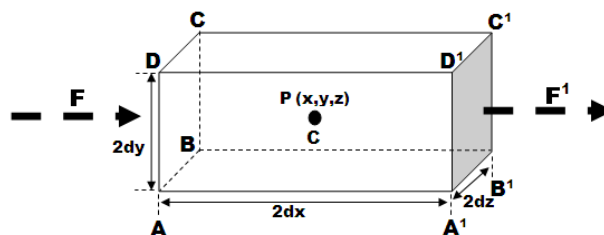

Figure 2-3:   *Schematic representation of a rectangular bar used to derive Fick's law* [4].

Suppose that at the center, $P(x, y, z)$, of the bar, the concentration of the diffusing substance is C. The amount of the diffusing substance entering the bar through the $ABCD$ face in the $x - dx$ plane is given by;

$$4dydz(F_x - \frac{\partial F_x}{\partial x}dx) \tag{2-2}$$

In equation 2-2, F_x is the rate of transfer through a unit area of the corresponding plane through P. The amount of diffusing substance lost through the face $A^1B^1C^1D^1$ is given by;

$$4dydz(F_x + \frac{\partial F_x}{\partial x}dx) \tag{2-3}$$

Equation 2-2 minus 2-3 gives;

$$-8dxdydz(\frac{\partial F_x}{\partial x}) \tag{2-4}$$

Similarly from the other faces we obtain equations 2-5 and 2-6;

$$-8dxdydz(\frac{\partial F_y}{\partial y}) \tag{2-5}$$

$$-8dxdydz(\frac{\partial F_z}{\partial z}) \tag{2-6}$$

The increase in the amount of diffusing substance in the element may be given by equation 2-7;

$$8dxdydz(\frac{\partial C}{\partial t}) \tag{2-7}$$

If the total amount of diffusing substance entering is equal to the increase in the amount of diffusing substance in the element, Equations 2-4, 2-5, 2-6 and 2-7 lead to equation 2-8;

$$\frac{\partial C}{\partial t} + \frac{\partial^2 F_x}{\partial x^2} + \frac{\partial^2 F_y}{\partial y^2} + \frac{\partial^2 F_z}{\partial z^2} = 0 \tag{2-8}$$

Equations 2-8 and 2-1 lead to equation 2-9;

$$\frac{\partial C}{\partial t} = D(\frac{\partial^2 C}{\partial x^2} + \frac{\partial^2 C}{\partial y^2} + \frac{\partial^2}{\partial z^2}) \tag{2-9}$$

If the diffusion is one-dimensional, i.e. if the concentration gradient is only in the x-direction; equation 2-9 becomes equation 2-10;

$$\frac{\partial C}{\partial t} = D\frac{\partial^2 C}{\partial x^2} \tag{2-10}$$

Equation 2-10 is called Fick's second law of diffusion [2, 4].

Quantitative measurements of the rate at which a diffusion process occurs is expressed in terms of the diffusion coefficient. For a diffusion process in one dimension, the diffusion coefficient may be defined as; the rate of transfer of diffusing substance across a unit of a section, divided by the space gradient of concentration at the section [3]. If the rectangular bar in figure 2-3 represents a pyrolytic carbon specimen, implanted with iodine, then equation 2-10 can be solved using equation 2-11 [5].

$$C(x,t) = \left[2(\pi Dt)^{1/2} \right]^{-1} \int_0^\infty C_0(y) \left[e^{-(y-x)^2/4Dt} + e^{-(y-x)^2/4Dt} \right] dy \qquad (2\text{-}11)$$

In equation 2-11, C is the concentration of iodine and t is time. At time $t = 0$, $C_0(x) = C(x,0)$ represents the initial iodine profile (i.e. the iodine profile before diffusion occurs). Measurements of the profile at $t=0$ can be approximated by the equation 2-12 [5].

$$C_0(x) = K(\pi Dt_0)^{-1/2} (e^{-x^2/4Dt_0}) \qquad (2\text{-}12)$$

In equation 2-12, K and t_0 are adjustable constants. Using the boundary condition, $\lim_{x \to 0} \frac{d}{dx} C(x,t) = 0$, and equation 2-12, equation 2-11 reduces to equation 2-13 [5].

$$C(x,t) = K[\pi D(t + t_0)]^{-1/2} [e^{\left(-x^2/4D(t+t_0)\right)}] \qquad (2\text{-}13)$$

If a profile $W(t)$ is defined in such a way that $C(W,t) = \frac{1}{2} C(0,t)$ then equation 2-13 becomes equation 2-14 [5];

$$[W(t)]^2 = 4Dt\ln(2) + [W(0)]^2 \qquad (2\text{-}14)$$

Equation 2-14 can be used to obtain the diffusion coefficient, D. A plot of $[W(t)]^2$ versus t yields the diffusion coefficient (slope). $[W(t)]^2$ is determined using the FWHM of the iodine peak. To obtain the activation energy E, the Arrhenius equation can be used [6].

$$D = D_0 \exp^{-E/kT} \qquad (2\text{-}15)$$

In equation 2-15, D is the diffusion coefficient, D_0 is the pre-exponential factor, E is the activation energy, T is the absolute temperature and k is the gas constant.

2.3   REFERENCES

[1]   B.L. Sharma. Diffusion in semiconductors, Vlg. Trans. Tech. Publications, Clausthal-Zellerfeld (1970).

[2]   D. Gupta. Diffusion in Bulk Solids and Thin Films: IBM, T. J. Watson Research Center, Yorktown Heights, New York. (2005).

[3]   P.L. Walker. Chemistry and Physics of carbon, A series of advances. **5** Marcel Dekker, Inc, New York (1969).

[4]   J. Crank. Mathematics of diffusion, 2nd edition. Oxford University Press, Oxford. (1975).

[5]   S.M. Myers, S.T. Picraux and T.S. Prevender. Phys. Rev. B**9** (1974) 3953-3964.

[6]   S.P. Murarka. Diffusion Barriers in Semiconductor Devices / Circuits. Rensselaer Polytechnic InstituteTroy, New York (2006).

CHAPTER 3:   PYROLYTIC CARBON (PyC)

3.1   PROPERTIES OF PYROLYTIC CARBON

Pyrolytic carbon (PyC) is a carbon material obtained from the decomposition and dehydrogenation of gaseous hydrocarbons (methane, propylene, acetylene, ethylene, etc.) in an activated environment. The fluidized–bed chemical vapor deposition (FB-CVD) process is used to produce the pyrolytic carbon layers for nuclear reactor TRISO fuel particles; see Figure 3-1 [1, 2]. The precursors or source materials used during the deposition of the porous PyC buffer layer, with density of approximately 1.10 to 1.20 g.cm^{-3}, is usually acetylene. The deposition temperature may range between 300 °C and 750 °C at 1 atm. For the dense pyrolytic carbon (the second and fourth layer from the uranium kernel in the nuclear fuel), methane (CH_4) is commonly used. Deposition temperatures of about 1800 °C to 2000 °C produce PyC (inner and outer) with approximately 1.70 to 1.90 g/cm^3 density [3].
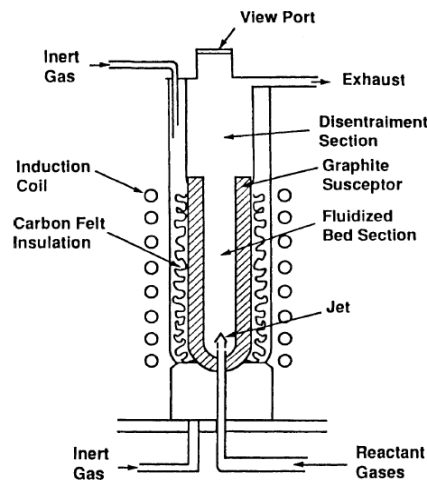

Figure 3-1:   *Schematic representation of FB-CVD [1, 2].*

In this section, the following will be discussed; the properties of pyrolytic carbon, the various structures of pyrolytic carbon, and the characterization of the structures of PyC. The properties of PyC are very similar to those of single crystal graphite, where carbon atoms form continuous hexagons in stacked basal planes (a-b directions); see Figure 3-2. In each basal plane, the carbon atom is bound to its three neighbors by strong covalent bonds. This type of bonding is called sp^2 hybrid bonding. The hybridized fourth valence electron is bounded to an electron on the adjacent plane by a much weaker Van der Waal's bonds. The

spacing between the basal planes is 0.335 nm and the distance between nearest atom centers in the basal planes is 0.142 nm [4, 5].
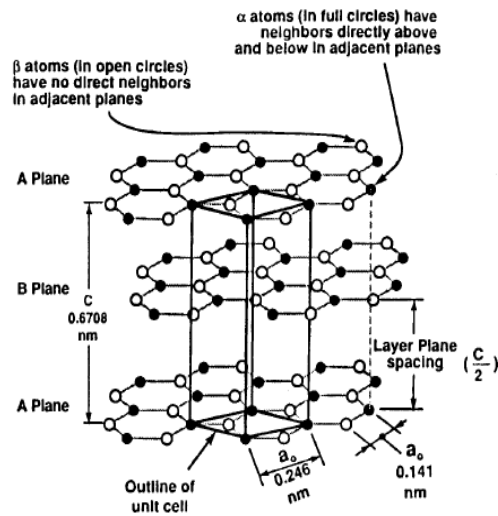

Figure 3-2:   *Structure of a graphite crystal [2, 5]. In this study, the layer plane spacing ($C/2$) is called the interlayer spacing and will be represented by the letter d. The dimension C=0.6708 nm will be represented by the notation L_c.*

PyC differs from graphite in that its crystal layers vary in perfection and contain single or multiple vacant lattice sites. Not all layers are arranged parallel to each other. Some structures deposited at relatively low temperatures contain single unassociated layers, small fractions of amorphous carbon, or substantial amounts of hydrogen. This type of structure is sometimes called a 'turbostratic structure'. The crystalline size, density, anisotropy/isotropy and preferred orientation vary depending on deposition conditions; see Figure 3-3 (b) [6].
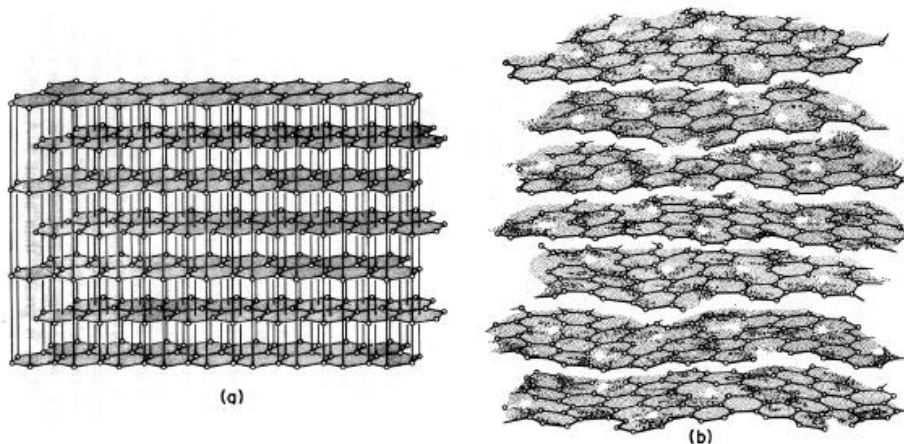

Figure 3-3:   *Schematic diagrams comparing (a) a 3-dimensional graphite lattice with, (b) a laminar PyC structure [6].*

FB-CVD deposits produce four different types of microstructures depending on deposition conditions such as deposition temperature, contact time, composition and quantity of the precursor, and the bed surface area. The microstructures are characterized as laminar, isotropic, granular, and columnar [7]. The densities of all these structures vary between 1.5 and 2.1 g.cm^{-3}.

The laminar structures are formed at deposition temperatures below 1500 °C. The crystalline properties are anisotropic (see Figure 3-4 (b) - high) and have a moderate to high degree of preferred orientation; see Figures 3-4 (a). These structures are known to be less stable under heat treatment and neutron irradiation compared to other forms.

Figure 3-4:   *(a) Relationship between anisotropy factor, apparent crystalline size (L_c) and bed (deposition) temperature [7]. (b) Illustration showing degree of preferred orientation in PyC structures. High represents a structure with high degree of anisotropy [7]. The bed temperature in this figure refers to temperature (deposition temperature) used during preparation of the PyC samples using FB-CVD while the annealing temperature in figure 3-6 refers to the heat treatment after the PyC samples have been prepared.*

In Figure 3-4 (a), the apparent crystallite size is the crystallite size as measured using XRD, which may sometimes be different from the true crystallite size [8].

The anisotropy factor is used to measure the degree of preferred orientation of the graphitic layers. A value close to 1 indicates a low degree of preferred orientation, implying an isotropic structure. On the other hand, the higher from 1 the value becomes, the higher the degree of preferred orientation. So in Figure 3-4 (b), a PyC with high degree of preferred orientation will be represented by 'high' while 'isotropic' represents a PyC with a lowest degree of preferred orientation.

The isotropic structures are formed at intermediate deposition temperatures above 1500 °C. As the name suggests, these structures are highly isotropic; see Figures 3-4 and 3-5. The crystallites in this type of structures are randomly oriented (very low preferred orientation). Under heat treatment, they show much less interlayer slippages characteristic of the laminar structures. They are therefore much harder and have much better wear resistance than the other microstructures. They are also much superior in that they have better impermeability to gases. The isotropic microstructures are regarded as the most suitable pyrolytic carbons for nuclear reactor applications. They have density of approximately 2.1 g. cm^{-3} when a methane precursor is used [7].

Figure 3-5:   *The relationship between microstructures of PyC and FB-CVD temperature. The y-axis represents CH$_4$ concentration and the x-axis represents deposition temperature in degree Celsius [7].*

The granular structures are formed at high deposition temperatures (above $\approx$ 1700 °C) and low precursor concentrations (less than 10%); see Figure 3-5. They have low to moderate anisotropy as well as low to moderate degree of preferred orientation. They are called granular when the grains are small and nearly randomly oriented.

The columnar structure has similar properties as the granular structure, but the grains are larger and more aligned with the growth direction. The crystallites are deposited with the basal planes essentially parallel to the deposition surface. Their structure tends to be columnar (cone-like) as a result of uninterrupted grain growth toward the reactant source [5, 6, 7, 9, 10].

3.2   PROPERTIES OF PYROLYTIC CARBON AFTER HEAT TREATMENT (ANNEALING)

For PyC deposited at 600 °C to 900 °C, heat treatment can cause the release of H_2 and other gaseous products, which results in the contraction of layer planes. The release of H_2 is due to the dehydrogenation of large condensed aromatic molecules which are present in the layers of poorly crystalline, low temperature carbons after deposition. Heat treatment will therefore cause structural changes in the microstructures of such PyC [5].

Under heat treatment the apparent crystallite size increases from the one obtained after deposition; see Figure 3-6. The laminar structures tend to graphitize (i.e. become more like the graphite structure). This is due to the re-ordering of layers in the structure, i.e. the basal planes become more parallel and closer to each other. Vacancies, dislocations, stacking faults and rotational disorders tend to heal and disappear.

Figure 3-6 shows that post deposition heat treatment causes an increase in the apparent crystallite size. This means that after heat treatment of the PyC samples, the apparent crystallite size becomes greater than the apparent crystallite size measured just after they were prepared. For example Figure 3-4 shows that a PyC sample prepared by FB-CVD using bed temperature of between 1700 and 1800 °C will have an apparent crystallite size (initial) of approximately 40 Å. If the same PyC sample is annealed at 1700 °C, Figure 3-6 shows that the apparent crystallite size will increase to just above 80 Å.
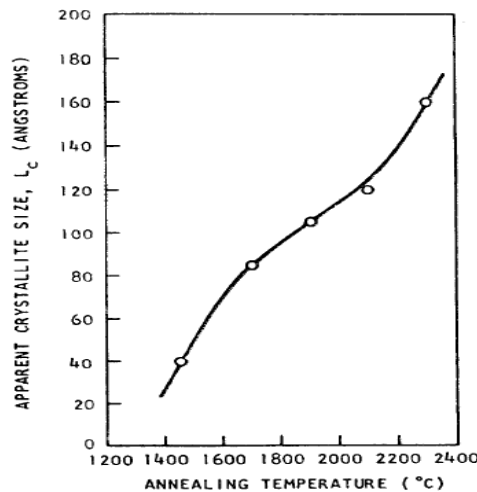
Figure 3-6:   *Effect of annealing on apparent crystalline size of laminar pyrolytic carbons deposited at 1400 °C [7]. The annealing temperature in this figure refers to the heat treatment after the PyC samples have been prepared while bed temperature in Figure 3-4 refers to temperature (deposition temperature) applied during preparation of the PyC samples using FB-CVD.*

Figure 3-7 indicates that the interlayer spacing (d ~ 3.47 Å) for PyC decreases with higher annealing temperatures to approach that of the ideal graphite crystal (d ~ 3.35 Å) [7]. Since graphite has a high degree of preferred orientation, therefore annealing at 2800 °C will result in an increase in preferred orientation (anisotropy) of the isotropic PyC structure. Hence, the structure becomes similar to that of highly oriented pyrolytic graphite (HOPG), which is less stable under heat treatment and neutron irradiation.
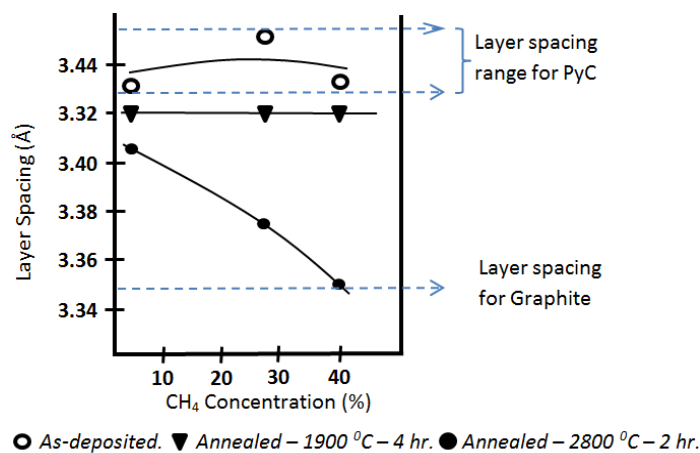

Figure 3-7:   *Effect of annealing on layer spacing of pyrolytic carbon [7].*

Other effects of heat treatment on PyC are densification (see Figure 3-8), dimensional changes, and changes in isotropy / anisotropy of the PyC [7].
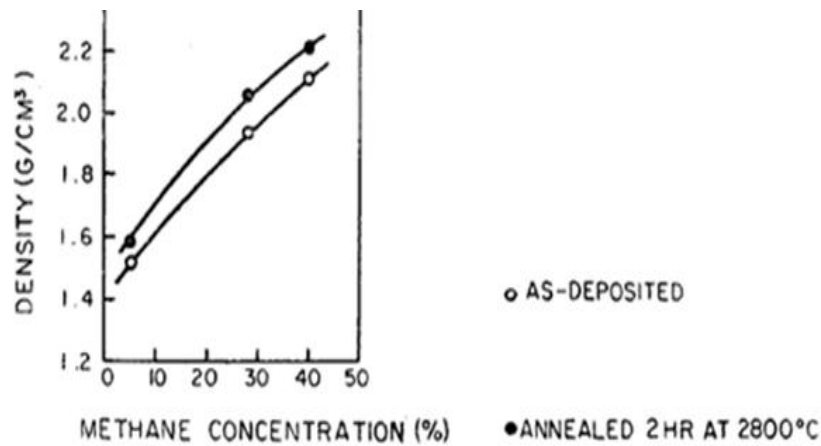

Figure 3-8:   *Effect of annealing on the density of laminar pyrolytic carbon [7].*

3.3   CHARACTERISATION OF THE MICROSTRUCTURE OF PyC

The microstructure of PyC depends on the deposition conditions as well as post deposition heat treatment or annealing. The fundamental parameters that determine the microstructures of pyrolytic carbons to be discussed in this study are; crystallite size, crystallite layer spacing, isotropy / anisotropy and preferred orientation [6]. X-ray diffraction is a very useful tool in the characterization of the microstructures of pyrolytic carbon. It can provide quantitative data on the layer spacing, crystallite size (mean layer diameter and height of crystallites), and the degree of preferred orientation of layer planes. The measurement of the $C_{(002)}$ diffraction peak will be useful to quantify the above.

3.3.1   Crystallite Size (See figure 3-6)

The crystallite size or apparent crystallite size can be found using the Scherer equation [6] given by;

$$L_c = \frac{0.94\lambda}{B_{(00l)}\cos\theta}$$

(3-1)

In equation 3-1, λ is the wavelength, θ is the diffraction angle and $B_{(00l)}$ is the full width at half maximum (FWHM) of the $(00l)$ peak or reflection used, and L_c is the apparent crystallite size.

3.3.2   The Inter-Layer Spacing

The inter-layer spacing reported for many PyCs deposited by FB-CVD at 1200 to 2200 °C is approximately 3.44 Å, and has been accepted to be the ideal inter-layer spacing for completely disordered layers in soft carbons. The inter-layer spacing, d_{hkl} is given equation 3-3 [6];

$$d_{hkl} = \frac{n\lambda}{2\sin\theta} \qquad \text{[Bragg's law]} \qquad (3\text{-}3)$$

In equation 3-3, λ is the wavelength and θ is the diffraction angle.

3.3.3   Preferred Orientation

Figure 3-9:   *Illustration of preferred orientation in (a) an isotropic PyC (ISO-PyC) and (b) highly oriented PyC [6]. C_(002) peak intensity produced by HO-PyC is higher than that produced by ISO-PyC.*

The effect of heat treatment on preferred orientation can be determined using XRD. The intensity of the $C_{(002)}$ lattice planes provides a good indication of whether the degree of preferred orientation increases or decreases after heat treatment. Previous studies have shown that the higher the intensity of the $C_{(002)}$, the higher the degree of preferred orientation [6]. Therefore from Figure 3-9, the $C_{(002)}$ intensity produced by the isotropic PyC will be lower than that produced by highly oriented PyC (HO-PyC).

3.4   MICROSTRUCTURE OF THE PyC LAYERS IN TRISO PARTICLES

The research group working on nuclear materials has characterized the microstructure of the PyC layers used in the TRISO particles using a variety of techniques. Using SEM they found that the PyC layers have cavities to absorb gaseous fission products and to accommodate thermal and mechanical shocks to the TRISO particle; see Figure 3-10. Furthermore, the PyC layers are composed of spheres often with smaller cavities near them; see Figure 3-11. As can be seen from Figure 3-12, these spheres have an inner laminar structure.

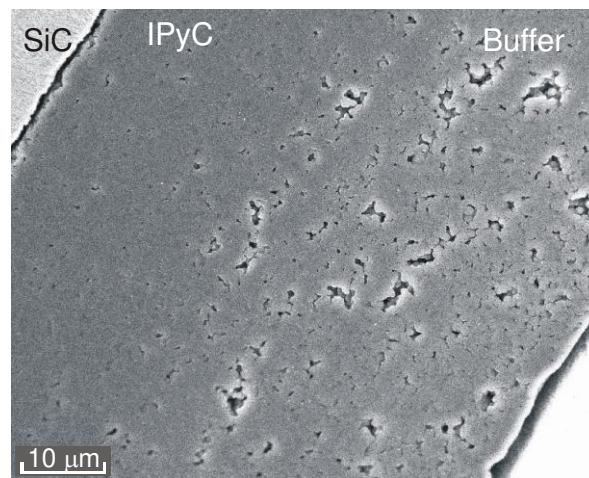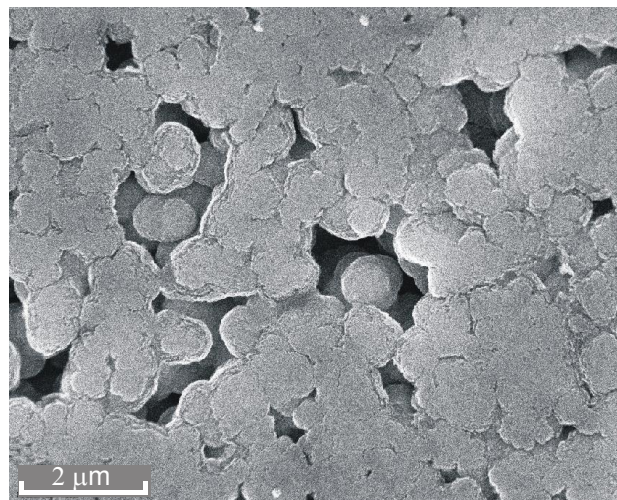**Figure 3-10:** *An SEM image of the buffer (porous carbon) and I-PyC layer of a TRISO particle* [11].

Figure 3-11: *SEM image to demonstrate that the microstructure of the PyC layers in the TRISO particle consists of carbon spheres and pores* [11].
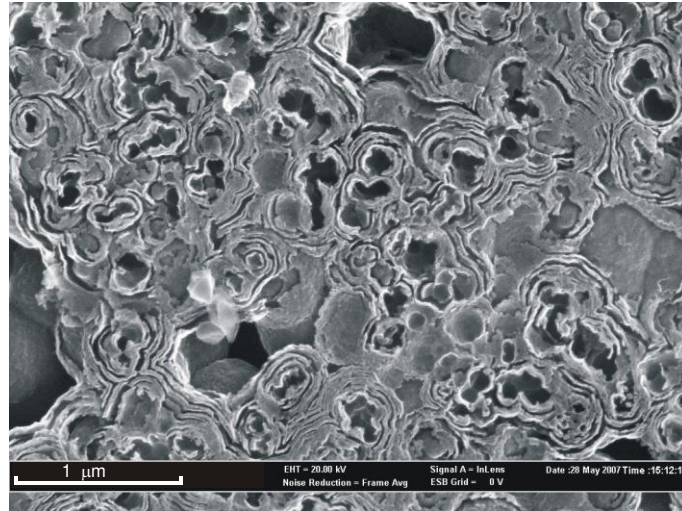
Figure 3-12: *An SEM image of a polished and chemically etched PyC layer showing the laminar inner microstructure of the carbon spheres.* [11].

3.5   REFERENCES

[1]   E. Lopez-Honorato, P.J. Meadows and P. Xiao. Carbon **47** (2009) 396-410.

[2]   P. Morgan. Carbon Fibers and their Composites, Taylor and Francis (2005).

[3]   L.H. Ford, N.S. Hibbert and D.G. Martin. J. Nucl. Mater. **45** (1972-73) 139-49.

[4]   H.O. Pierson. Handbook of Carbon, Graphite, Diamond and Fullerenes - Properties, Processing, and Applications, William Andrew Publishing / Noyes (1993).

[5]   H.O. Pierson. Handbook of Chemical Vapor Deposition-Principles, Technology and Applications, 2nd edition, William Andrew Publishing / Noyes (1999).

[6]   P.L. Walker. Chemistry and Physics of carbon, A series of advances. **5** Marcel Dekker, Inc, New York (1969).

[7]   J.C. Bokros and R.J. Price. Carbon **3** (1966) 503-519.

[8]   J.I. Langford and A.J.C. Wilson. J. Appl. Cryst. **11** (1978) 102-113.

[9]   L. Vesetini, G. Pellegrini, G. Saracco, and I. Zubani. J. Nucl. Mater. **52** (1974) 157-166.

[10]   R.J. Price, J. Bokros, K. Koyama, and J. Chin. Carbon **3** (1966) 263-272.

[11]   N.G. van der Berg, J.B. Malherbe, A.J. Botha, E. Friedland, and W.A. Jesser, Surf. Interface Anal. **42** (2009) 1156 -1159; *ibid* 1377.

CHAPTER 4:   EXPERIMENTAL TECHNIQUES

4.1   RUTHERFORD BACKSCATTERING SPECTROMETRY (RBS)

RBS played a major role in the study of the diffusion behavior of iodine in pyrolytic carbon. It was used to investigate the distribution profiles of iodine as a function of depth below the surface of pyrolytic carbon specimens. This was achieved by irradiating the iodine implanted specimens with a beam of He^+ ions, and the backscattered beam was analyzed. The experimental setup is shown in Figure 4-1, and a summary discussing the functions of the main components follows.
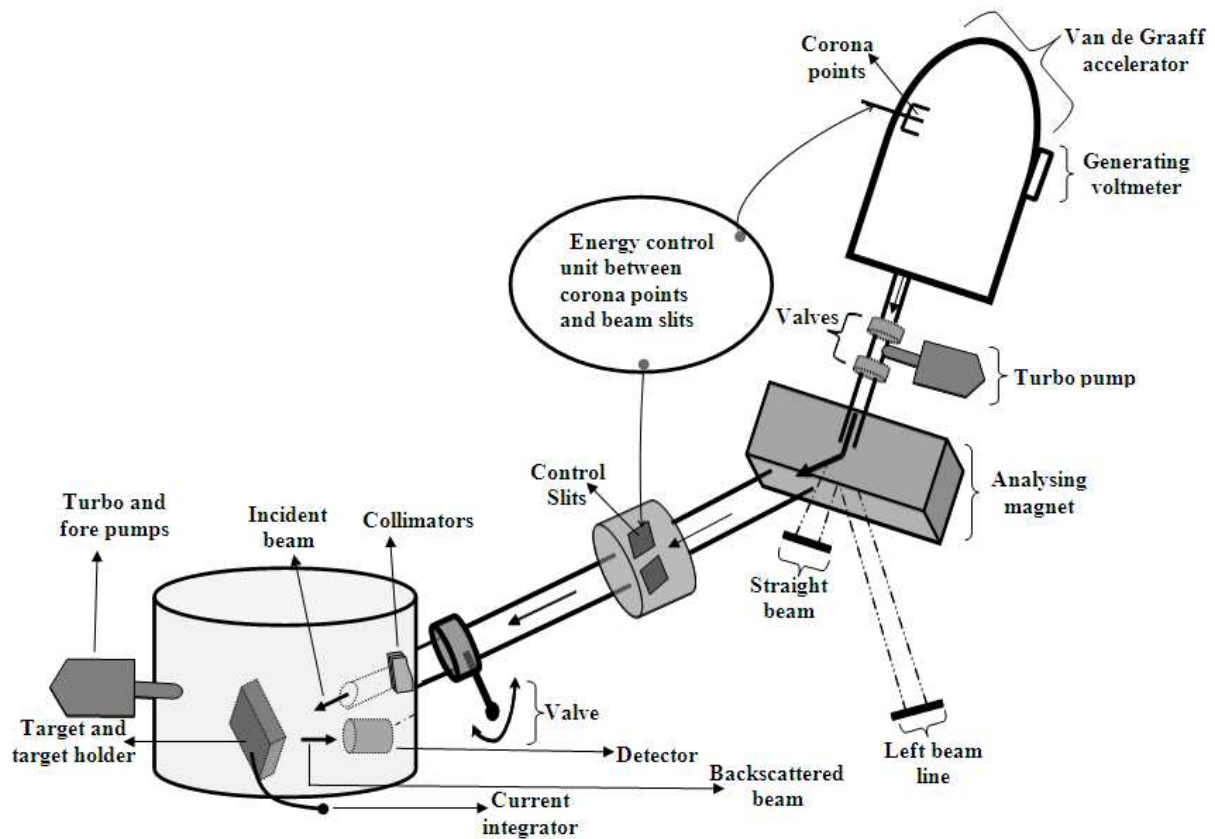

Figure 4-1:   *The RBS set up at the physics department at the University of Pretoria.*

In order to produce a beam of He^+ particles inside the Van de Graaff accelerator (shown in Figure 4-2), an ionization chamber consisting of helium gas is used to ionize the gas into He^+ ions using radio frequency energy. A positive voltage is applied in the terminal shell to

accelerate the He^{+} ions from the ion source into and through the evacuated acceleration path or accelerator tube. This voltage is produced and maintained in the terminal shell by means of a charge belt which is constantly moving to convey charge between ground potential and the terminal. Corona points were used to stabilize the terminal voltage with a feedback system from the beam slits, by creating a discharge path between them and the high voltage terminal shell. High vacuum was always maintained in the accelerator tube in order to minimize interaction between the beam and molecules in the vacuum. Surrounding the accelerator tube is a tank, which was first evacuated and then filled with a combination of dry gases (CO_2 and N_2) at a pressure of 340 psi [1].

Figure 4-2: *The Van de Graaff accelerator* [1].

After leaving the accelerator, the beam passes through an analyzing magnet, slits, and collimators before it enters the high vacuum target chamber. The analyzing magnet is set up such that only a beam of required energy (e.g. 1.6 MeV) passes through it. The slits and collimators were used to control the size and direction of the beam. The entrance into the target chamber was controlled using a valve that could be manually opened and closed. When the beam became incident on the PyC specimen, some ions were backscattered into the detector as a result of scattering with carbon atoms in the PyC substrate while others were backscattered as a result of scattering with the implanted iodine. An electron suppression device was used to suppress electrons that are emitted from the target as secondary electrons to improve the current integrator [1]. The distribution of the implanted iodine before and after

annealing is analyzed using the backscattered He$^+$ ions that become incident on the detector. Inside the semiconductor detector, the particles produce electron-hole pairs, the number of which is proportional to the energy of the particles. Subsequently, the current pulses produced by the detector are used to infer the energy of the backscattered particles. The detector output is then amplified using the pre- and main amplifiers and fed to the multichannel analyzer (MCA), which records the number of backscattered ions with energies in successive intervals or channels [2]. The data from the MCA is then passed on to the PC where it is analyzed; see Figure 4-3.

Figure 4-3:   The data acquisition and analysis section in the RBS set up at the University of Pretoria.

In data analysis, a plot of yield versus channel number is developed resulting in a backscattering spectrum. The data can be analyzed using RUMP, Genplot, SIMNRA, M.S. Excel programs and other relevant software programs.

4.1.1   Analysis of RBS results

In order to accurately read and analyze the data produced by the backscattered ions, a summary of the manner in which the incident ions interact with atoms inside the substrate is necessary. The following information discusses the backscattering process and the concepts used to analyze the measurement results. Concepts such as the kinematic factor, the scattering cross section, energy loss, stopping cross section, depth resolution and energy straggling; were used to analyze the results.

4.1.1.1   Qualitative analysis: Identifying peaks in an RBS spectrum

Qualitative analysis was performed on the obtained measurement results in order to identify the target atoms associated with the peaks in the spectra. By definition, the energy of backscattered particles is given by equation 4-1 [2], where E_0 is the energy of the incident He^+ particles, E_1 is the energy of the backscattered He^+ particles and K is the kinematic factor [2] and is given by equation 4-2.

$$E_1 = KE_0 \tag{4-1}$$

$$K = \left\{ \frac{\left[1 - (M_1 \sin\theta/M_2)^2\right]^{1/2} + (M_1 \sin\theta/M_2)}{1 + (M_1/M_2)} \right\}^2 \tag{4-2}$$

The kinematic factors for the elements of interest, i.e. carbon and iodine, were calculated using equation 4-2. They are derived from the concept of a two body collision between a projectile with mass M_1 and an atom at rest with mass M_2, where the principle of conservation of kinetic energy and momentum is applied. An illustration of this collision is shown in the Figure 4-4.

Figure 4-4: *Schematic representation of an elastic collision between an incident particle and a target atom, where kinetic energy and momentum are conserved [1].*

The principles of conservation of kinetic energy and momentum are applied and for an elastic collision to occur, the following conditions must be satisfied. The energy E_0 of the incident particle must be greater than the binding energy between atoms. Nuclear reactions and resonances must not occur; for example, the H^+ particle can produce nuclear reactions at

energy below 1MeV and He$^+$ particles can produce nuclear reactions at energy ranging between 2 to 3MeV depending on the target atom species [1].

A full derivation of the equation for the kinematic factor is provided in Reference 1. In this study, M_1 is represented by the incident beam of He$^+$ ions and M_2 is represented by either the carbon atoms or the iodine atoms. The angle θ shown in Figure 4-4 is called the scattering angle (165°). Using equations 4-1 and 4-2, it is possible to produce qualitative results for any given RBS spectrum. A plot of backscattered energy versus channel number was created and used to calibrate the surface positions of carbon and other elements. The backscattered energy was compared to corresponding channel numbers, using incident beams with energy of 1.6 MeV and 1.4 MeV. The resulting slope (keV / channel) of the graph was used to determine the energy calibration of the detector system.

It was simple to identify the peaks associated with the elements of interest, *viz.* carbon and iodine because our specimens consisted of only carbon and the implanted iodine. There was however a low concentration peak corresponding to oxygen that appeared in all spectra. This peak appeared in all the samples before and after heat treatment.

4.1.1.2   Quantitative analysis: Calculating the number of iodine atoms after implantation and heat treatment

In order to accurately reveal how iodine behaves in PyC, it was necessary to monitor the number of implanted iodine atoms after heat treatment and compare with the number before heat treatment. This made it possible to determine the loss of iodine atoms after each heat treatment. The total number of iodine atoms per unit area in the PyC substrate was calculated using equation 4-3 [1].

$$N_I = \frac{\rho_A}{\sigma.\Omega.Q} \tag{4-3}$$

In equation 4-3, N_I is the areal density used to determine the number of target atoms per unit area, ρ_A is the number of detected particles and is determined by taking the integral of the area under the iodine peak, Q represents the total number of incident particles, *i.e.* the applied charge divided by 1.6×10^{-19} C and Ω represents the detector solid angle which can be physically measured or calculated using equation 4-4 [1].

$$\Omega = \frac{[\varepsilon_0]\cos\theta_1}{\sigma.Q.\xi.H_0} \qquad (4\text{-}4)$$

In equation 4-4, H_0 is the carbon edge whose height in counts is obtained from the spectrum, ξ is the energy width of a channel (eV/Channel) and is obtained from calibration, $[\varepsilon_0]$ is the stopping cross section factor at the surface (surface approximation) and was obtained from the tables in Chu *et al.* [1] and θ_1 is the incidence angle.

In equations 4-3 and 4-4, σ represents the average scattering cross section and is used to determine the probability that a collision will lead to scattering, and that the scattered particle will reach the detector. It is defined by equation 4-5 [1].

$$\sigma = \frac{1}{\Omega}\int_\Omega \left(\frac{d\sigma}{d\Omega}\right) d\Omega \qquad (4\text{-}5)$$

The differential scattering cross section, $\frac{d\sigma}{d\Omega}$, and the average scattering cross section, σ, will be used to determine the above mentioned probability [1].

The differential scattering cross section can be defined by considering a narrow beam of He^+ particles incident on a sample wider than the beam; see Figure 4-5. Suppose that some of the incident particles are scattered at an angle, θ, and that the detector counts the scattered particles at a solid angle $d\Omega$, as shown in Figure 4-5.
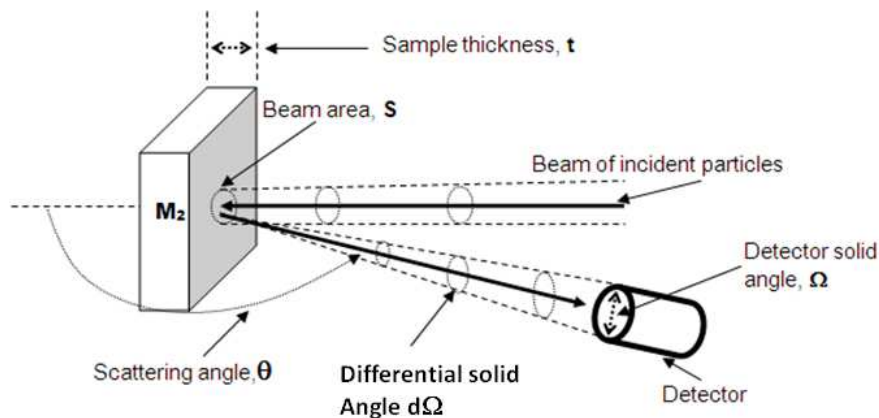

Figure 4-5:   *Scattering experiment to demonstrate the concept of the differential scattering cross section [1].*

If Q is the total number of particles that strike the target and dQ the number of particles counted by the detector or the number of particles backscattered into the solid angle $d\Omega$ [1], the

differential scattering cross section is therefore defined by equation 4-6 [1], where $\frac{d\sigma}{d\Omega}$ is the differential scattering cross section and can be used to determine the probability that a collision will lead to scattering, and that the scattered particle will reach the detector.

$$\frac{d\sigma}{d\Omega} = \frac{1}{Nt}\left[\frac{(dQ/d\Omega)}{Q}\right] SNt\left(\frac{d\sigma}{d\Omega}\right) \qquad (4\text{-}6)$$

In equation 4-6, N is the volume density of atoms in the target material, t is the target thickness; Nt is the number of target atoms per unit area. Equation 4-6 is valid only if $d\Omega$ is small enough to allow a good definition of the angle θ and the target slice must be sufficiently thin to neglect the energy loss of the projectiles. If S be the surface area of the target illuminated uniformly by the beam, then SNt is equivalent to the number atoms eligible for scattering collision in the target. Hence, $SNt(d\sigma/d\Omega)$ represents the total cross sectional area of all eligible atoms. The probability that the scattering event will be recorded by the detector depends on the ratio of $SNt(d\sigma/d\Omega)$ to S. In order for an elastic collision to occur between an incident particle and the nuclei of the target atom, the distance of closest approach between the two must be sufficiently large compared to nuclear dimensions but small compared with the Bohr radius, $a_0 = \hbar/m_e e$. The formula for the differential scattering cross section is given by equation 4-7 [1];

$$\left(\frac{d\sigma}{d\Omega}\right)_c = \left[\frac{Z_1 Z_2 e^2}{4E\sin^2(\theta/2)}\right]^2 \qquad (4\text{-}7)$$

In equation 4-7, c is the center of mass coordinate, Z_1 is the atomic number of the projectile with mass M_1, Z_2 is the atomic number of the target atom with mass M_2, e is the electronic charge, and E is the energy of the projectile immediately before scattering. Equation 4-7 can be transformed from center of mass to laboratory reference leading to equation 4-8 [1];

$$\frac{d\sigma}{d\Omega} = \left(\frac{Z_1 Z_2 e^2}{4E}\right)^2 \frac{4\left\{\left[1-\left((M_1/M_2)\sin\theta\right)^2\right]^{1/2}\right\}^2}{\left[1-\left((M_1/M_2)\sin\theta\right)^2\right]^{1/2}} \qquad (4\text{-}8)$$

Some conclusions can be made from the differential scattering cross section about the behavior the incident He^+ particles and the target carbon atoms during the scattering process. Firstly, $\frac{d\sigma}{d\Omega}\alpha\, Z_1^2$ implies that the backscattering yield obtained from a target atom with a He^+ ($Z_1=2$) incident beam is four times larger than with a proton beam ($Z_1=1$). A carbon beam is nine times larger than the He^+ incident beam. Secondly, $\frac{d\sigma}{d\Omega}\alpha\, Z_2^2$ implies that Rutherford

backscattering spectrometry is much more sensitive to heavy elements than the lighter elements. Thirdly, $\frac{d\sigma}{d\Omega} \alpha \frac{1}{E^2}$ implies that the yield of scattered particles rises rapidly with decreasing energy of the incident particles [1].

4.1.1.3   Depth profiling: Determining iodine depth into the PyC substrate after implantation and heat treatment.

When the iodine atoms are implanted into the PyC substrate, they penetrate the substrate and come to rest somewhere deeper inside it. When the substrate is annealed at temperatures much higher that room temperature, the iodine atoms may become mobile again and the initial depth after implantation may change. As part of studying the behaviour of iodine in PyC, the iodine depth profile in PyC was monitored before after each heat treatment. An RBS spectrum is usually presented as yield (counts) versus channel numbers. In order to carry out diffusion studies, it is necessary to analyze the depth at which backscattering events occur inside the target. This requires that a depth scale be used instead of channel numbers. This was achieved using the known energy loss and stopping power of He in solids.

When a beam of ions penetrates a substrate, electronic or nuclear stopping may occur. Electronic stopping occurs when the ions from the beam collide with target electrons and nuclear stopping occurs when they collide with target nuclei [3]. At low ion energies (typically lower than 100 keV), nuclear stopping is dominant, whereas at higher energies, electronic stopping becomes dominant. As the beam travels through the substrate both in the inward and the outward paths, it slows down and its kinetic energy decreases. This means that, as the beam travels a distance Δx into the substrate, it loses an energy ΔE along the inward path. The energy loss per unit length (specific energy loss) is defined as $\lim_{\Delta x \to 0}(\Delta E/\Delta x) \equiv (dE/dx)(E)$ for that particular particle and energy in the substrate, also referred to as the stopping power [1, 3].

The relationship between the energy difference ΔE_1 (i.e. $KE_0 - E_1$ in Figure 4-6) and depth x at which the particle is scattered from is given by equation 4-9 [4]; where $[S]$ is called the energy loss factor.

$$\Delta E_1 = [S]x \qquad\qquad (4\text{-}9)$$

The energy loss factor is defined by equation 4-10 [4].

$$[S] = \frac{K}{\cos\theta_1}\left(\frac{dE}{dx}\right)_{E_{in}} + \frac{1}{\cos\theta_2}\left(\frac{dE}{dx}\right)_{E_{out}}$$ (4-10)

The values of $\frac{dE}{dx}$ are given in terms of the stopping cross section $\varepsilon \equiv (\frac{1}{N})(\frac{dE}{dx})$ or $\varepsilon^* \equiv (\frac{1}{\rho})(\frac{dE}{dx})$

with $\rho = N(\frac{M}{N_0})$ where M is the atomic weight (g/mole), N_0 = 6.025 x 10 [23] is Avogadro's

number, N is the atomic density, and ε is called the stopping cross section [1, 4]. E_{in} is a

representative value of E along the inward path and E_{out} is a representative value of E along

the outward path. Shown above is the mean approximation, which is a more accurate method.

The surface energy approximation is valid for thin or small depths.

From the backscattering event shown in Figure 4-6, an incident beam of, say He^{+} ions, has

energy E_0. When the ions are backscattered near the surface, they will have energies

approximated by KE_0 (K is the kinematic factor) and when backscattered at some depth x into

the substrate, they will have energy E_1.

Figure 4-6:   *Description of backscattering events near the surface of the target as well as*
            at depth x into the target [1].

The depth from which the He^{+} ions are backscattered can be estimated using equation 4-11 [2].

A depth profile of the implanted iodine could therefore be estimated.

$$E_1 = KE_0 - [S]x$$ (4-11)

The values for the energy loss as well as the stopping cross section are given in Chu *et al.* [1]

and Ziegler [5].

4.1.2   Electronic and Nuclear stopping

The concepts of electronic and nuclear stopping describe the behavior of incident projectiles as they travel into and out of the target material. Nuclear stopping occurs as a result of angular scattering collisions of incident particles with nuclei of atoms in the target material. Electronic stopping occurs as a result of slight loss of energy the incident particles experience as it scatters from the cloud of electrons surrounding the target atoms. When the energy of the bombarding particle is low nuclear stopping is dominant, while electronic stopping is dominant at higher energies, as shown in Figure 4-7.
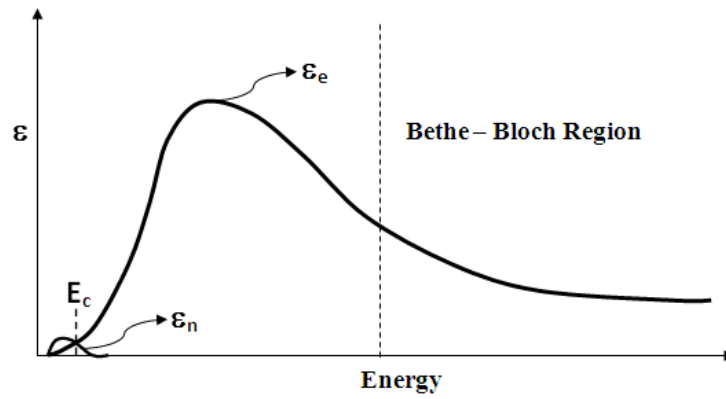

Figure 4-7:   *Dependencies of electronic (ε_e) and nuclear (ε_n) contributions to the stopping cross section ε as a function of the energy E of the incident particle* [1].

The electronic energy loss can be calculated using equation 4-12 [1].

$$\left. \frac{dE}{dx} \right|_e = NZ_2 \left[\frac{4\pi \left(Z_1 e^2 \right)^2}{m_e v_1^2} \right] \ln \left(\frac{b_{max}}{b_{min}} \right) \qquad (4\text{-}12)$$

Z_1e is the charge of the projectile, v_1 is the velocity of the projectile, Z_2e is the charge of the target particle, N is the atomic density, and b_{min} and b_{max} describe the impact parameter of the incident particles and the target atoms. At high energies beyond the maximum of the electronic stopping region, the Bethe-Bloch equation provides a better estimation of the electronic energy loss (stopping), as shown in equation 4-13 [1].

$$\left. \frac{dE}{dx} \right|_e = NZ_2 \left[\frac{4\pi (Z_1 e^2)^2}{m_e v_1^2} \right] L \qquad (4\text{-}13)$$

In equation 4-13, $L = \ln\left(2m_e v_1^2 / I\right)$ is called the stopping number and 'I' is an average over the various excitations and ionizations of the electrons in a target atom. In this study, He$^+$ ions were used at higher energies (1.6 MeV). In this case, these ions lose energy primary as a result of electronic energy loss [1].

4.1.3   Energy straggling

When a beam of energetic particles is incident on a homogeneous target with thickness Δx and is subsequently transmitted through it, the energy loss as a result of interactions with atoms inside the target is subject to fluctuations, i.e. the particles in the transmitted beam do not have the same energy distribution and this results in broader peaks in RBS spectra; see Figure 4-8. This phenomenon is referred to as energy straggling. The consequence of energy straggling is that the energy E of the transmitted particles is no longer mono-energetic. As a result, the ratio E_1 / E_0 as well as the identification of M_2 can become uncertain. This affects the approximation of depth resolution for implanted species [1].
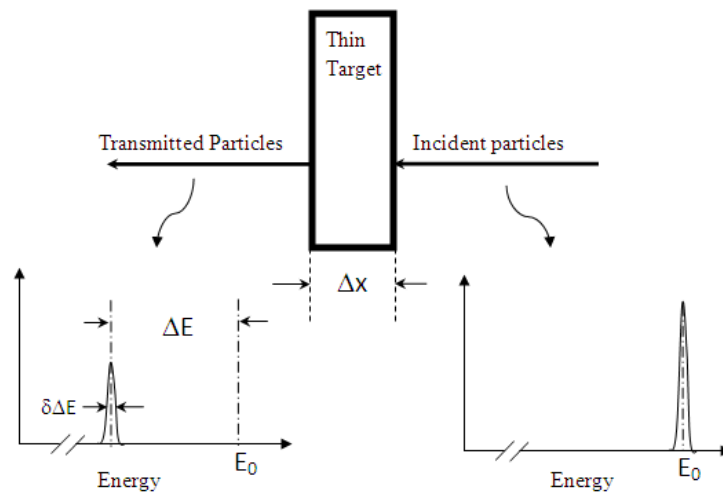

Figure 4-8:   *Illustration of energy straggling when a mono-energetic beam of energy E_0 loses energy ΔE in traversing a thin film of thickness Δx. Energy straggling broadens simultaneously the energy profile* [1].

In this study, a beam of He$^+$ ions in the MeV range is used to study diffusion. The energy loss will therefore primarily be due to interactions with electrons in the PyC target. Hence, the dominant contribution to energy straggling would be from electronic energy loss. Equation 4-14 shows the energy straggling formula [1].

$$\left\langle (\delta \Delta E)^2 \right\rangle = N Z_2 \Delta x \, 2\pi \frac{(Z_1 e^2)^2}{m_e v_1^2} (E_{max} - E_{min}) \qquad (4\text{-}14)$$

E_{min} and E_{max} are the energy losses corresponding to encounters with minimum and maximum impact parameters. The largest possible energy transfer in a collision between the ion of mass M_1 and an electron of mass $m_e \ll M_1$ is $2m_e v_1^2$, so that if $E_{min} \ll E_{max}$, then equation 4-14 transforms into equation 4-15 [1].

$$\left\langle (\delta \Delta E)^2 \right\rangle = N Z_2 \, 4\pi (Z_1 e^2)^2 \Delta x \qquad (4\text{-}15)$$

Equation 4-15 is called the Bohr value Ω_B^2 of energy straggling. For a layer of thickness t, Bohr straggling thus has the variance, $\Omega_B^2 = 4\pi(Z_1 e^2 N Z_2 t)$, which leads to equation 4-16 [1]; where $s^2 = 4\pi(Z_1 e^2)^2 N Z_2$.

$$\Omega_B^2 = s^2 t \qquad (4\text{-}16)$$

Bohr's theory predicts that energy straggling does not depend on the energy of the projectile and that the RMS value of the energy variation increases with the square root of the electron density per unit area $N Z_2 t$ in the target [1].

4.2   ION IMPLANTATION

In order to study the diffusion of iodine in PyC, iodine ions were introduced beyond the surface of the PyC samples. Ion implantation is the process where ionized iodine is introduced into the PyC substrate with enough energy to penetrate beyond the surface. In this study, iodine ions were implanted into PyC substrates at room temperature. Advantages of ion implantation include the capability of precisely controlling the number of implanted iodine atoms and the dopant's depth distribution profile. This can be determined using concepts such as specific energy loss, atomic cross-section, electronic stopping and nuclear stopping.

4.2.1   Specific energy loss / Stopping power.

Section 4.1.2 discussed the two types of energy losses that result when charged atoms are incident on a target, i.e. nuclear energy loss and electronic energy loss. Refer to figure 4-7. Since the energy of the incident He^+ ions used in this study are in the MeV range, attention

was directed to electronic energy loss. In ion implantation, nuclear energy loss became dominant. The incident iodine ions were bombarded onto the PyC substrate at lower energies (360 keV). They slow down and came to rest as a result of nuclear energy loss [4]. The specific energy loss or stopping power in nuclear stopping is due to collisions of the iodine ions with the nuclei of the PyC atoms, and is defined using elastic two-body scattering model, leading to equation 4-17 [6] as follows;

$$-\left(\frac{dE}{dx}\right) = N\Delta x \int_0^\infty T(E,p) 2\pi p \, dp \tag{4-17}$$

T represents the energy transferred from the incident ions to the struck atoms and p is the impact parameter. The energy transfer $T(E,p)$ may take any value between zero (for $p = \infty$) and a maximum value given by $T_m = [4M_1 M_2/(M_1 + M_2)]E_1$.

4.2.2   Range / Ion depth distribution.

When iodine ions are incident on the PyC substrate, they undergo scattering events with electrons and atoms in the substrate, reducing the ion's energies until they come to rest. The total path length the ions travel until the come to rest is called the range. Dearnaley *et al.* [6] defines the range as follows; 'When the energy of an ion falls to about 20 eV it ceases to move through the solid, becoming trapped by the cohesive forces of the material, and the total distance travelled from the surface to this point is called the (total) range. Since the ions do not follow a straight route before coming to rest, it is necessary to define the total range, R_{tot} and the projected range R_p. The projected range is the average distance a group of implanted ions travel into the surface. The relationship between the total range and the specific nuclear energy loss is given by [4];

$$R_{tot} = \int_0^E \frac{dE}{-(dE/dx)}$$

Neglecting electronic energy loss leads to an energy-independent specific energy loss given by equation 4-18 [6] as follows;

$$R_{tot} = \frac{0.6(Z_1^{2/3} + Z_2^{2/3})^{1/2}(M_1 + M_2)M_2 E}{Z_1 Z_2 M_1} \tag{4-18}$$

The constant 0.6 is introduced so that if E is measured in keV, R_{tot} is given in micrograms of target per cm^2. The projected range can be estimated using equation 4-19 [6] given as follows;

$$\frac{R_{tot}}{R_p} = \frac{1}{4}[(5+A)\frac{1+A}{2A}\cos^{-1}\frac{1-A}{1+A} - 1 - 3A] \tag{4-19}$$

$A = M_2/M_1$ and for $M_2 < M_1$, equation 5.4 becomes $\dfrac{R_{tot}}{R_p} \approx 1 + \dfrac{M_2}{3M_1}$. At low energies, an alternative approach for estimating the range by neglecting electronic energy loss can be used by determining the mean range [4], $\overline{R}(E_0)$, i.e.

$$\overline{R}(E_0) = \lambda(E_0) + (E_0)^{-1/2} \int_0^{E_0} \lambda(E) E^{-1/2} dE \qquad (4\text{-}20)$$

$$\lambda(E) = \frac{1}{4}\pi N r^2(E)$$

During implantation, the incident iodine ions do not travel in a straight path inside the PyC as a result of straggling. Straggle is the standard deviation of the range or the mean square fluctuation in range. The range straggling is obtained from the mean square fluctuation in energy loss, leading to the following equation [6].

$$\overline{\Delta R^2} = N\Omega^2 (\frac{d\overline{R}}{dE})^3 dE \qquad (4\text{-}21)$$

$$\Omega^2 = \int_0^{T_m} T^2 d\sigma(T)$$

The mean square fluctuation in the total range is given by the following integral;

$$\overline{\Delta R_{tot}^2} = \frac{1}{N^2} \int_0^{E} \frac{\Omega(E)dE}{(d\overline{R}/dE)^3} \qquad (4\text{-}22)$$

For pure electronic stopping, $\qquad \overline{\Delta R_{tot}^2} = \int_0^{E} 4\pi N e^2 Z_1^2 (dE/dx)^{-3} dE \qquad (4\text{-}23)$

The Bethe-Bloch straggling formula for low-mass absorbers is given as follows [6];

$$S_{tr} = \frac{\overline{\Delta R_{tot}^2}}{\left(\overline{R_{tot}}\right)^2} = 4m/M_1 \ln(2m\upsilon^2/I) \qquad (4\text{-}24)$$

The Bethe-Bloch straggling formula for heavy-mass absorbers is given as follows;

$$S_{tr} = 3m/4M_1 \qquad (4\text{-}25)$$

This treatment of straggling assumes, as a first approximation, that the range distribution is Gaussian. In other words, the probability distribution P(R) of range is given by [6];

$$P(R)dR = \frac{1}{2\pi}\left(\overline{\Delta R^2}\right)^{1/2} \exp-(\frac{R-\overline{R}}{2\Delta R^2}) \qquad (4\text{-}26)$$

In this study, to predict the range or depth of distribution of the implanted iodine atoms, a simulation using the Transport of Ions in Matter (TRIM 2008) [7] was performed with the same conditions as the ones used during ion implantation of iodine in PyC. The depth in nm produced by the TRIM simulation was used to predict the iodine depth into the PyC substrate

after implantation. It was also compared with one calculated using the method described in 4.1.1 and was found to be consistent.

4.2.3   Radiation damage in PyC during ion implantation.

One of the main disadvantages of ion implantation is that it usually causes some alterations in the original structure of the substrate, in this case the PyC. This is a disadvantage in applications where it is desired that the substrate maintains its original structure after ion implantation. In cases where the structural damage caused by ion implantation is similar to that caused by neutron irradiation, it may not necessarily be a disadvantage for a scientific study on radiation damage as this may resemble the conditions that the PyC undergoes during the operation of a nuclear plant. A number of text books discuss a number of types of damages due to ion implantation, such as atomic displacement, surface sputtering, etc. In this section, radiation damage on PyC as explained experimentally by Tanabe is discussed [8].

As discussed in chapter 2, the degree of preferred orientation depends on, among others, the deposition temperature and the amount of precursor used. The PyC materials with high degree of preferred orientation have a structure which is very close to the perfect graphite structure but with small defects. During ion irradiation, some carbon atoms become displaced resulting in defects along the basal planes as well as between the basal planes. Some of the carbon atoms lose their original sp^2 bonding and form new sp^3 bonding. The lattice space between the basal planes increases. An increase in ion dose results in growth of the defects along the basal planes and between them as well as an increase in formation of sp^3 clusters. The graphitic layers ultimately lose their ordering, resulting in open spaces. This results in a considerable decrease in the degree of preferred orientation of the graphitic layers and the surface layer of PyC becomes amorphous. Annealing the PyC after ion implantation may repair the structure back to its original form only for slightly damaged PyC specimens. Studies have shown that in general, it is not possible for heavily damaged PyC specimens to completely regain their original structure after annealing. A number of papers reporting on radiation damage of PyC due to ion implantation have already been published [8, 9].

4.3   X-RAY DIFFRACTION

4.3.1   The X-ray Diffraction Spectrometer.

The X-ray diffraction spectrometer is controlled mainly by a goniometer which is used to measure diffraction angles as well as a number of electronic circuits for determining the intensity of the diffracted X-rays at any angle [10]; see Figure 4-12. X-rays are generated inside the X-ray tube. A current is applied on the filament to release electrons. These electrons are accelerated towards the target by applying a voltage between the filament and the target. Upon striking the target, the electrons interact with the target atoms and energy is released in a form of X-ray photons.
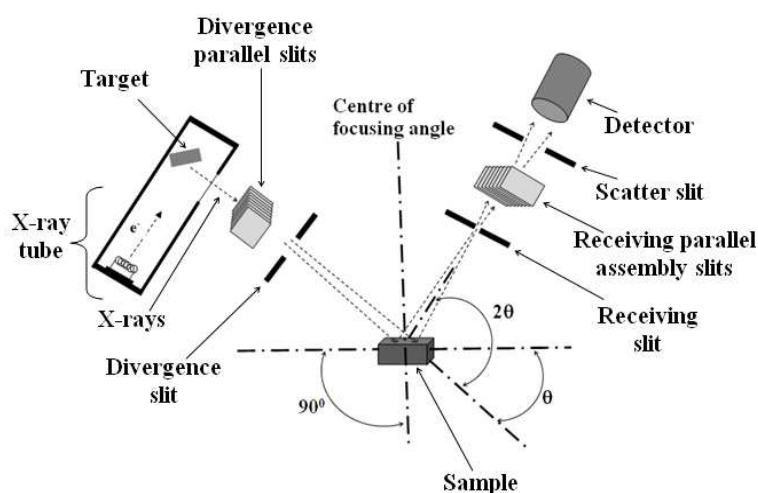

Figure 4-12: *The X-ray optical system showing the main components of an X-ray diffraction spectrometer [10].*

The X-rays exit the X-ray tube through a very thin window (usually made of beryllium). They pass through one set of parallel collimators / slits and a divergence slit before reaching the sample. The function of the divergence slit is to control the angular aperture of the X-ray beam. When the beam reaches the sample it is diffracted as shown in Figure 4-12. It then passes through a receiving slit, a set of receiving collimators / slits, and scatter slit. The function of the scatter slit is to exclude unwanted radiation, reducing the background of the spectrum. Eventually, the beam enters the detector and the produced pulses are counted [10, 11].

4.3.2   Diffraction of X-rays in crystals

When an X-ray is incident on an atom, it interacts with its electrons in two ways, i.e. it can be scattered or absorbed. When it is absorbed, secondary X-rays are produced. X-ray diffraction occurs as a result of those X-rays that are scattered. During the scattering process, the atomic nucleus, because of its relatively large mass, makes negligible contribution to the scattering of X-rays. The intensity of the scattered X-rays depends on the number of electrons associated with the nuclei, the electron distribution, the angle of scattering, and temperature. When a beam of X-rays is incident on a crystal, the X-rays are simultaneously scattered by the ordered atoms in all directions. The scattered X-rays will then interfere with one another constructively or destructively. Constructive interference occurs as a result of in-phase interference between two or more waves. The waves combine to form new wave fronts (illustrated in Figure 4-9). On the other hand, destructive interference occurs as a result of out of phase interference between two or more wave fronts. The angle or direction of diffraction of X-rays depends on the shape and size of the unit cell involved. The intensity of the diffracted X-rays depends on the kind of arrangement of atoms in the crystal [12].

In the case of the PyC materials used in this study, the intensity of the diffracted X-rays depended on the degree of preferred orientation of the graphitic layers. The higher the degree of preferred orientation of the graphitic layers, the higher the intensity of the diffracted X-rays. This phenomenon was used to study the behavior of the graphitic layers after heat treatment, which was then compared with the rate of loss of implanted iodine atoms from the PyC materials. Diffraction of X-rays occur according Bragg's law as given by the equation;

$$n\lambda = 2d_{hkl}\sin\theta \tag{4-27}$$

The symbol λ represents the X-ray wavelength, n is the order of reflection, $d_{(hkl)}$ is the lattice inter-layer spacing (for example the $C_{(002)}$ used in this study), and θ is the angle of reflection of the planes [12-14]. See Figure 4-9.

A number of studies have made use of the $C_{(002)}$ lattice plane reflections to characterize the structures PyC [11,13]. See Figures 4-10 and 4-11. Based on these findings, this study will investigate whether the degree of preferred orientation of graphitic layers influences the diffusion rate or the rate at which iodine is released from the PyC.
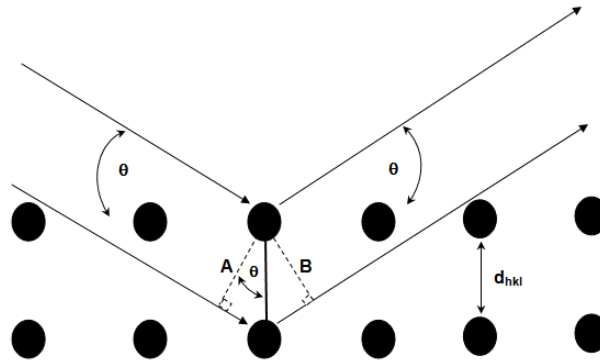
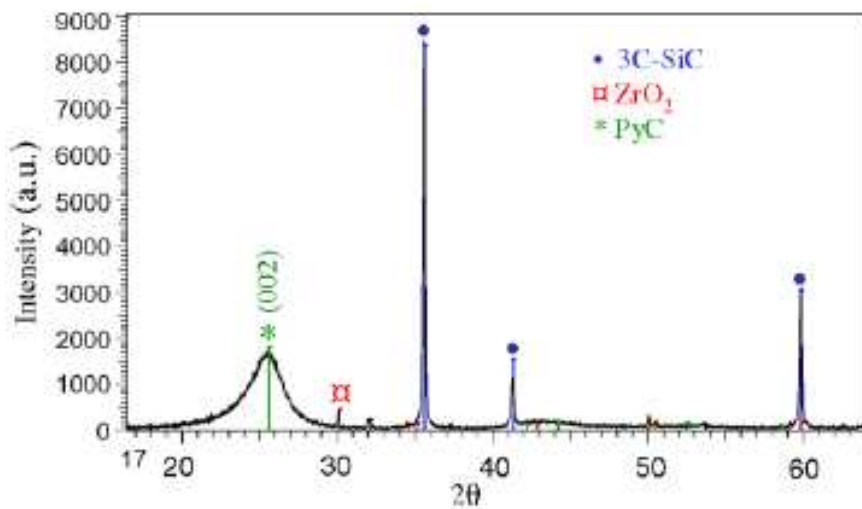**Figure 4-9:**   *Reflection of X-rays from two adjacent planes of atoms* [12].

Figure 4-10:   *X-ray diffraction pattern (green) of PyC, showing the C(002) lattice planes reflection* [11].

In Figure 4-10, the XRD spectra were obtained from a TRISO particle with a ZrO_2 kernel, the low density PyC layer (buffer), the inner dense pyrolytic carbon layer (I-PyC), the silicon carbide (SiC) layer and the outer dense pyrolytic carbon layer (O-PyC). The gas precursors consist of C_2H_2 for the buffer, C_3H_6 or C_2H_2/C_3H_6 for the dense PyC, and CH_3SiCl_3 for the SiC. The coatings are deposited at a temperature of 1300 to1400 °C for PyC and 1500 to 1600 °C for SiC. The XRD spectra were obtained using Cu Kα radiation from a Cu anode. The Scherrer relation and Bragg's law were used respectively to determine L_c and $d_{C(002)}$ spacing. The particles were measured directly (all particles are in the same plane) [11].
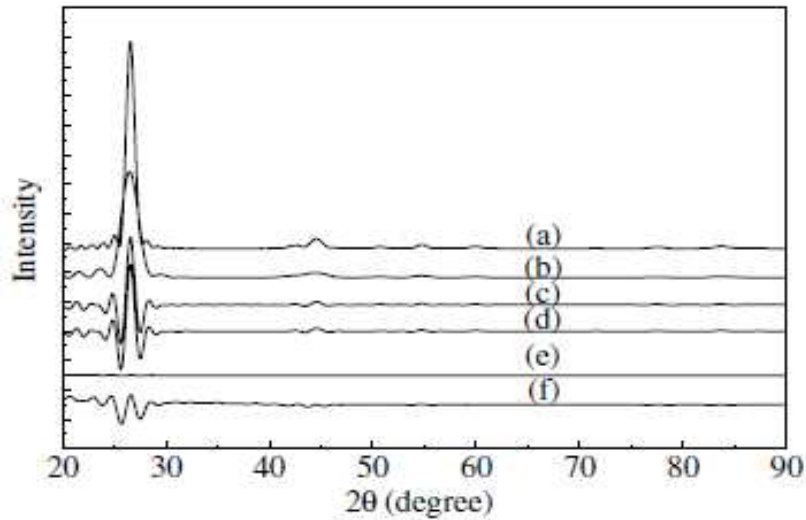
Figure 4-11: *Simulated X-ray diffraction patterns of PyC crystallites, showing the $C_{(002)}$ lattice planes reflections. (a) XRD pattern of crystallite A (L_a = 7.630 nm, L_c = 7.379 nm); (b) XRD pattern of crystallite B (L_a = 4.184 nm, L_c = 4.025 nm); (c) Difference plot between (a) and (b); (d) XRD difference plot obtained from $NDID_A$ - $NDID_B$; (e) Difference plot between plots (c) and (d); (f) An enlarged view of (e) with a ×40 scale expansion* [15].

In Figure 4-11 (d), $NDID_A$ stands for the numeric density of interatomic distance for crystallite A, and $NDID_B$ stands for the numeric density of interatomic distance for crystallite B [15]. The aim of figure 4-11 is to show the position of the $C_{(002)}$ peak. Details about the NDID's are given in reference 14.

4.4   SCANNING ELECTRON MICROSCOPY

Scanning electron microscopy (SEM) was used in this study to determine the topography or surface features of the PyC specimens before and after ion implantation and annealing. The main aim was to monitor the PyC surfaces for cracks and other damages before and after implantation.

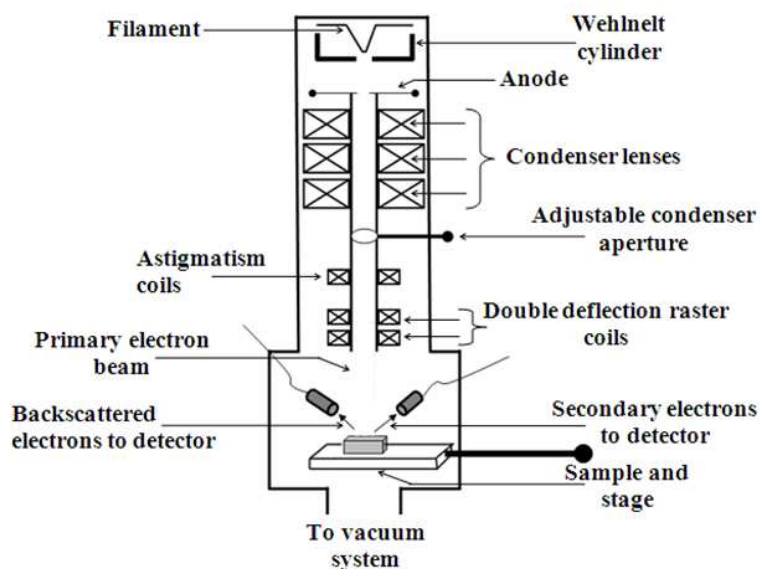### 4.4.1   The main components of an SEM

Figure 4-13: *Main components of an SEM microscope [16].*

As shown in Figure 4-13, the electron gun is used to generate a beam of electrons. It is composed of a filament or cathode made of a tungsten or LaB_6, a grid cap (Wehnelt cylinder) that controls the flow of electrons (bias), and a positively charged anode plate that attracts and accelerates the electrons out of the electron gun and down the column. A current is applied on the filament to release electrons and a voltage ranging between 0.1 to 40 kV can be applied between the filament and the anode to accelerate the electrons. Higher voltages result in better resolution but may generate greater heat which is not suitable for delicate specimens. A variable bias resistor is used to control the flow of electrons (beam current) that reach the sample.

Higher beam current lead to higher number of electrons that reach the sample. A higher voltage leads to deeper penetration depth [16]. The electron beam from the electron gun is controlled and directed toward the specimen by magnetic lenses. Electromagnetic lenses are used to de-magnify the image of the beam source exiting the electron gun and to focus the beam onto the sample [17]. Condenser lenses are used to reduce the size of the beams cross-over spot. Apertures are introduced into the beam path to reduce the effects of spherical aberration. Smaller apertures can be selected to achieve higher resolution, minimize beam scattering, and obtain smaller beam spot size on the sample [17].

When a beam of primary electrons reach the specimen, some electrons travel some distance into the specimen. Secondary electrons are produced as a result of inelastic collisions [15] where some of the primary electrons knock out electrons from energy levels of atoms in the specimen [14]. The secondary electrons have such low energy that they can only be detected when they are produced from the surface of the specimen. They are useful for topographical information and high resolution studies. Backscattered electrons are produced as a result of primary electrons being scattered in such a way that they escape back out of the specimen through the same surface they entered. Backscattered electrons are useful when atomic density and topographical information are required. In this study, secondary electrons were used to study the surfaces of the PyC samples. X-ray photons are emitted when electrons are knocked out from the atoms in the specimen. Other primary electrons may be transmitted through the specimen if it is thin enough [17].

The secondary electron detector (scintillation detector) was used to collect the secondary electrons coming from the surface of the specimen. The function of the photomultiplier is to amplify the original signal coming from the detector. The signal coming from the photomultiplier is converted to an image in the cathode ray tube (CRT). The image can be modified using the brightness and contrast controls, which are the main controls for setting up a micrograph [16, 17].

One of the most important features in the operation of an SEM is a good vacuum system. It prevents electrons from being scattered by collisions with unwanted molecules, resulting in a stable and controlled electron beam. The higher the vacuum, the better the microscope will operate.

4.5   REFERENCES

[1]   J. Chu, J.W. Meyer and M. Nicolet. Backscattering Spectrometry. Academic Press, Inc. (1978).

[2]   J.F. Romanelli, J.W. Mayer and E.J. Kramer. J. Polymer Sci. Polymer Phys. **24** (1986) 263-277.

[3]   M. Mayer. Rutherford Backscattering Spectrometry, Max-Planck-Institut fur Plasmaphysik, EURATOM Association, Garching, Germany (2003) 59-80.

[4]   M.B. Rogers. Rutherford Backscattering Spectroscopy, Institute of Synthetic Rubber Producers, Houston, TX Rim Association, Copley, OH. 8242-8247.

[5]   J.F. Ziegler. Helium stopping Powers and Ranges in all elements, Pergamon Press Inc. 3, New York (1977).

[6]   G. Dearnaley, J.H. Freeman, R.S. Nelson, and J. Stephen. Ion Implantation. **8** (1973) 9-221.

[7]   J.F. Ziegler, J.P. Biersack and Y. Littmark. The stopping and range of ions in solids, Pergamon Press, New York (1985).

[8]   T. Tanabe. Physica Scripta, **T64** (1996) 7-16.

[9]   D. Schroyen, M. Bruggeman, I. Dezsi, G. Langouche. Nucl. Instr. and Meth. in Phys. Res. **B15** (1986) 341-343.

[10]   E.W. Nuffield. X-ray diffraction methods, John Wiley and Sons, Inc, New York(1966).

[11]   D. Helary, O. Dugne, X. Bourrat. J. Nucl. Mater. **373** (2008) 150-156.

[12]   A.J. Dekker. Solid state physics, Macmilan, London (1963).

[13]   C. Hammond. The basics of crystallography and diffraction, Oxford University Press, New York **2** (2003).

[14]   H.T. Stokes. Solid state physics, Allyn and Bacon, Boston (1987).

[15]   Z.Q. Li, C.J. Lu, Z.P. Xia, Y. Zhou, Z. Luo. Carbon **45** (2007) 1686-1695.

[16]   M. Dunlap and J.E Adaskaveg. Introduction to the scanning electron microscopy Theory, Practice, and Procedures, facility for advanced instrumentation, U. C. Davis (1997).

[17]   B. Hafner. Scanning Electron Microscopy primer, Characterization Facility, University of Minnesota-Twin Cities (2007).

CHAPTER 5:   EXPERIMENTAL PROCEDURES

5.1   SAMPLE PREPARATION

Figure 5-1 shows the polished PyC samples with thickness of 3.2 mm purchased from 'SPI supplies'. They were sent (as received) to the University of Jena, Germany, for ion implantation. The conditions used to implant iodine into the PyC are shown in Table 5-1.
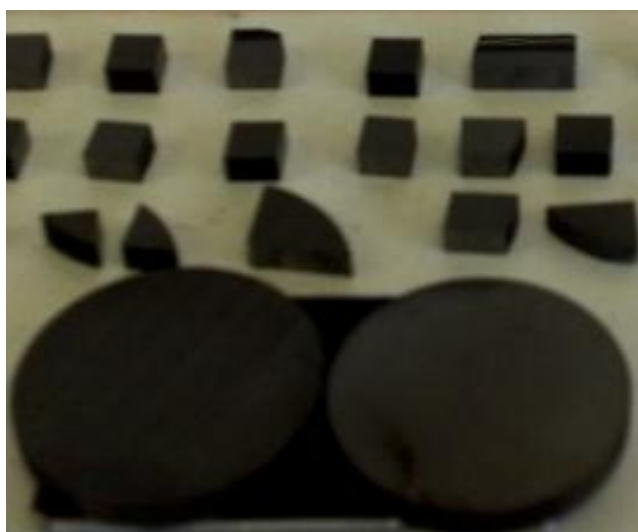

Figure 5-1:   *Polished PyC samples purchased from SPI supplies (Planchet student-tek); ref: www.2spi.com, LOT #1141109 3.2mm.*

Table 5-1:   *Conditions used in the implantation of iodine ions into PyC*

Fluence	Incident Energy	Temperature	Dose rate	Incident angle
1×10^{15} I^{+} cm^{2}	360 keV	Room Temperature (RT)	10^{13} cm^{-2}.sec	7° from sample normal

After implantation, the samples were cut into proper sizes to fit into the sample holders used in RBS, XRD and SEM. The cutting was done using an electric diamond plated copper blade. The samples were glued onto a brass piece and cut into smaller pieces. After cutting, the glue was washed off using acetone, deionized water and methanol. Figure 5-2 shows the importance of thoroughly rinsing the samples in de-ionized water after using acetone. It helps to remove the contamination as shown in Figure 5-2.
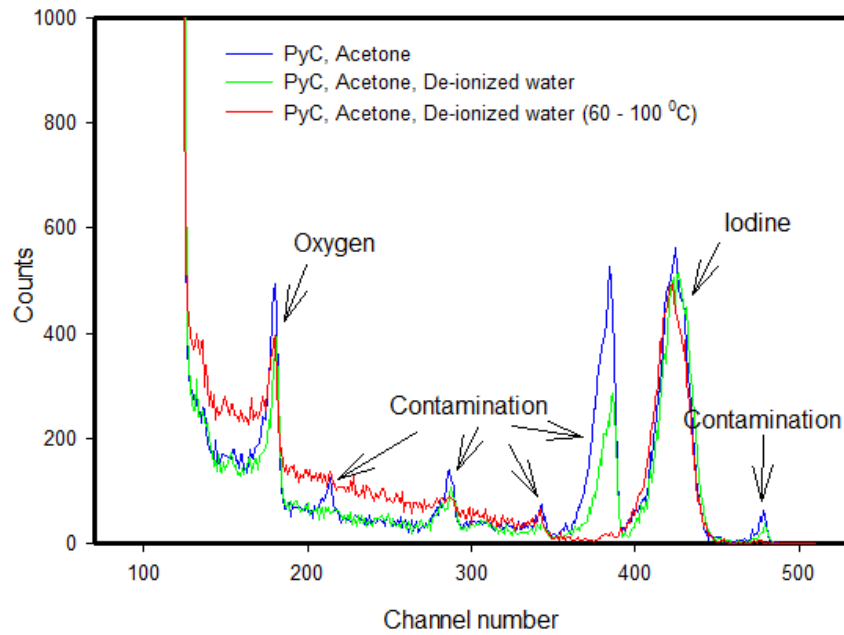
Figure 5-2:   *RBS measurements from a sample where the glue was washed off with only acetone, acetone and de-ionized water, and acetone and warm de-ionized water.*

5.2   ANNEALING / HEAT TREATMENT

After iodine implantation, the PyC samples were annealed at 900 °C, 1 000 °C, 1 100 °C and 1 200 °C, all for nine hours. A different PyC sample was used for each annealing temperature. The samples were loaded into graphite crucibles and annealed in vacuum for nine hours, using the WEBB 77 oven (RD Webb Company).
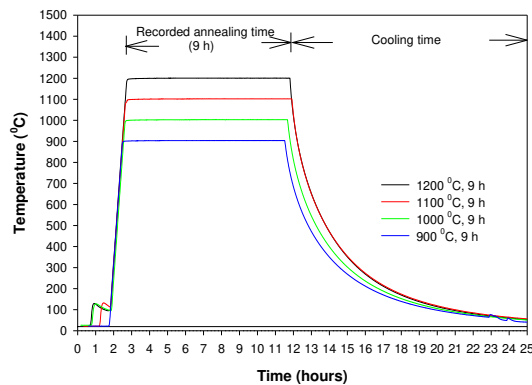

Figure 5-3:   *Temperature versus Time graph for the PyC samples showing how the annealing time was measured.*

Annealing studies of iodine implanted in pyrolytic carbon

Figure 5-3 is the temperature versus time graphs showing how the nine hour times were measured after annealing the samples. It also shows the cooling time to be much longer than the recorded annealing time.

5.3   MEASUREMENT CONDITIONS

5.3.1   RBS measurement conditions

The iodine implanted samples were measured using RBS before and after annealing at 900 °C, 1000 °C, 1100 °C and 1200 °C. The RBS measurement conditions used are given in Table 5-2. The samples were mounted inside a vacuum chamber and irradiated by the 1.6 MeV He^+ beam provided by a Van der Graaff's accelerator of the University of Pretoria. A charge of 120 µC was used. The overall detector plus electronic resolution of the system (FWHM) was of the order of 15 keV. A current of 20 nA and the scattering angle of 165° were used.

Table 5-2:   *RBS incident beam conditions used to measure the PyC samples before and after ion implantation and annealing.*

Incident beam	Energy	Charge	Current	Scattering angle (θ)
He^+	1.6 MeV	120 µC	20 nA	165°

5.3.2   XRD Measurement conditions

The XRD measurements were performed at ambient conditions using a Panalytical Xpert PRO, in θ-2θ configuration. All the samples were measured before and after annealing at 1000 °C, 1100 °C, and 1200 °C, using the conditions Table 5-3. An X-ray tube equipped with a cobalt (Co) anode material was used. A current of 50 mA and voltage of 35 kV was applied on the anode. As was the case with a number of literature, the $C_{(002)}$ peak was used to determine the influence of heat treatment on the degree of preferred orientation of the PyC graphitic layers [1-3].

Table 5-3:   *XRD measurement conditions used to measure the PyC samples before and after heat treatment.*

X-ray Tube			Scan Details			
Anode	Current (mA)	Voltage (kV)	Step Size (2θ)	Step Time (s)	Scan Start (2θ)	Scan End (2θ)
Cobalt (Co)	50	35	0.008°	5.5	10°	120°

5.3.3   SEM conditions for obtaining micrographs.

The surfaces of all samples were studied using the Zeiss Ultra Plus 55 FEG SEM using a voltage of 2 kV. SEM in-lens images were taken of surfaces of all samples before and after ion implantation and annealing, in order to determine changes in the surface microstructure and morphology brought about by the different treatments. The SEM conditions (e.g. magnification and mode) were kept constant for easy comparisons.

5.4   REFERENCES

[1]   E. Lopez-Honorato, P.J. Meadows, P. Xiao. Carbon **47** (2009) 396 – 410.

[2]   P.L. Walker. Chemistry and Physics of Carbon. **5** Marcel Dekker, Inc. New York (1969).

[3]   D. He´lary, O. Dugne, X. Bourrat. Journal of Nucl.Mat. **373** (2008) 150 – 156.

CHAPTER 6:   RESULTS AND DISCUSSION

6.1   SEM RESULTS

This section will show and discuss the results obtained using SEM. The SEM in-lens images were used mainly to identify any damages such as cracks as well as contamination on the polished surfaces of the PyC samples before and after cutting, implantation and annealing.

Figure 6-1 shows cracks that formed on the polished surface of some of the samples after cutting. Such cracks can detrimentally affect our other results. This was one of the reasons why the samples were analyzed with SEM before and after cutting as well as annealing, and only those samples that did not show cracks were used. These cracks also revealed flake-like structures lying nearly perpendicular to the polished surfaces; see also Figure 6-2 *(i)*. This indicated that the graphitic layers of the PyC are nearly perpendicular to the polished surface. This resulted in the decision to perform XRD measurements from the surface where the graphitic layers are parallel to the surface; in order to obtain the $C_{(002)}$ peak. This is discussed in more detail in section 6.2.
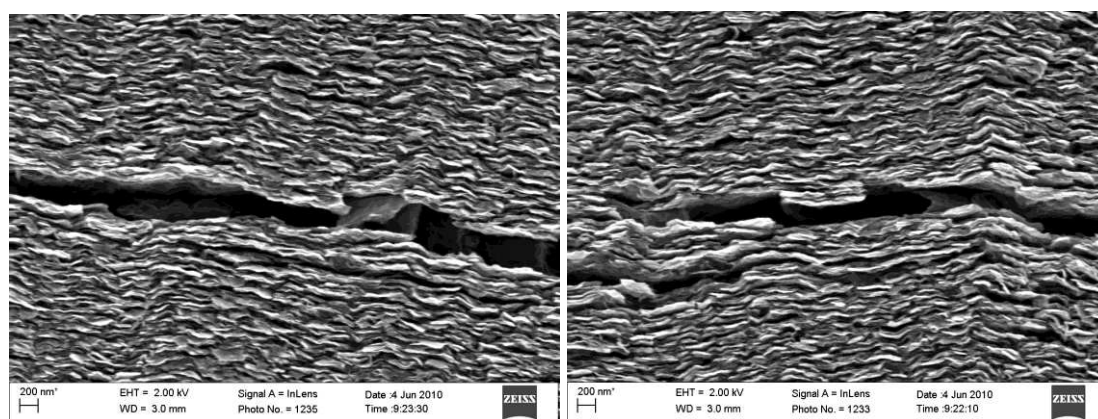

Figure 6-1:   *SEM images of some of the PyC samples with cracks after cutting.*

Figure 6.2 *(i)* show results from the as-received PyC sample. The supplier (SPI supplies) did not specify the deposition temperature. Figure 6-2 *(ii) (a)* shows results from an as-deposited PyC sample formed by chemical vapor deposition at 1100 °C by Guellali *et al.* [1]. Since Bokros *et al.* [2] reported that PyC specimens deposited at temperatures below 1500 °C produce laminar structures when a methane precursor is used, the similarities between the two sets of SEM images suggest that the samples used in our study could be laminar in

structure, deposited at temperature below or equal to 1500 °C, and could therefore have a medium to high degree of preferred orientation. As discussed in section 3.4, PyC with laminar structures are used in the design of TRISO particles.
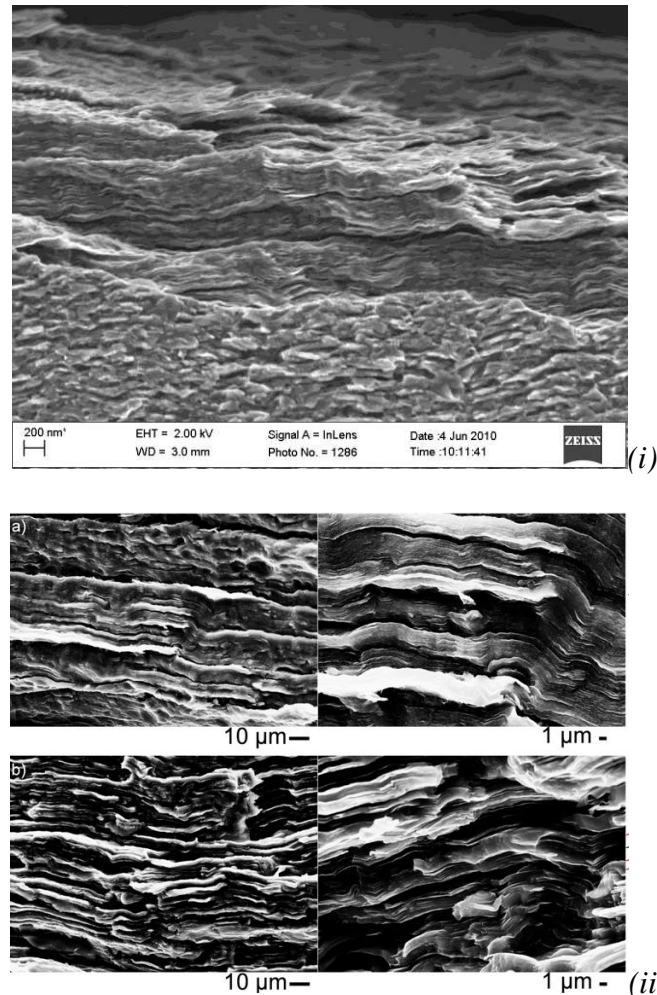

Figure 6-2:   *(i) An SEM micrograph from the surface of a typical PyC sample used in this study is compared with (ii) SEM micrographs from the fracture surface of a PyC (a) as deposited and (b) after heat treatment at 2900 °C; obtained by Guellali et al.* [1].

Figures 6-3 to 6-7 show the SEM images for the samples before and after annealing at 900 °C, 1000 °C, 1100 °C, and 1200 °C. Even though the PyC samples used in this study were not annealed up 2900 °C, those that were annealed at 900 °C, 1000 °C, 1100 °C, and 1200 °C do show some resemblance to Guellali *et al* [1] SEM micrographs (as shown in Figure 6-2 *(ii)* *(b))*. They both show the flake-like structures to be more compact for the as-deposited PyC than for the annealed PyC. There is also a systematic increase in crystallite sizes with

increasing annealing temperatures in line with the discussion in section 3.2. In a follow up study we shall use X-ray diffraction and the Scherrer equation to determine the crystallite sizes L_c of our annealed samples to quantify this (SEM) statement.
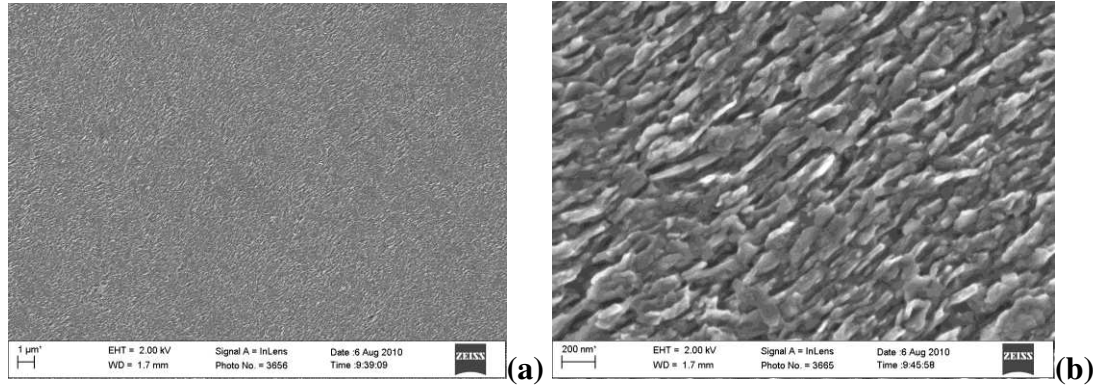

Figure 6-3:   *SEM images for as-implanted PyC. (a) Lower magnification with the size bar = 1 µm. (b) Higher magnification with the size bar = 200 nm.*
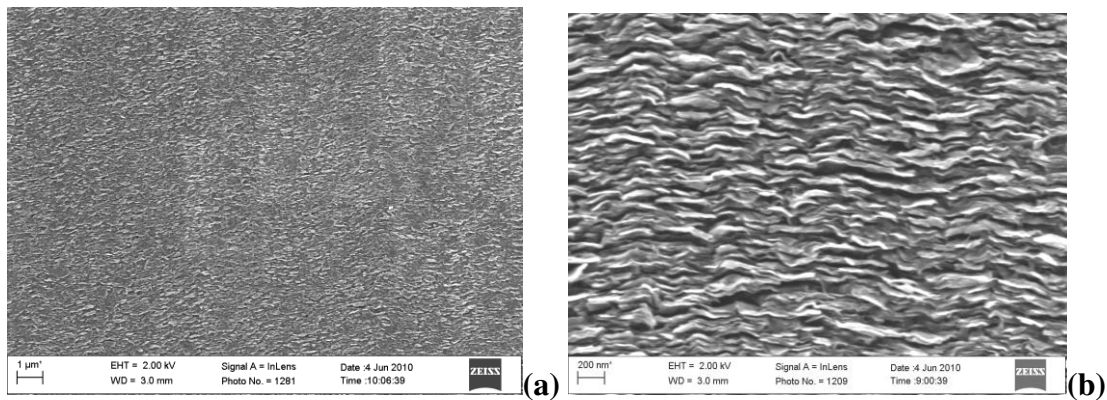

Figure 6-4:   *SEM images for PyC annealed at 900 °C for 9 hours. (a) Lower magnification with the size bar = 1 µm. (b) Higher magnification with the size bar = 200 nm.*
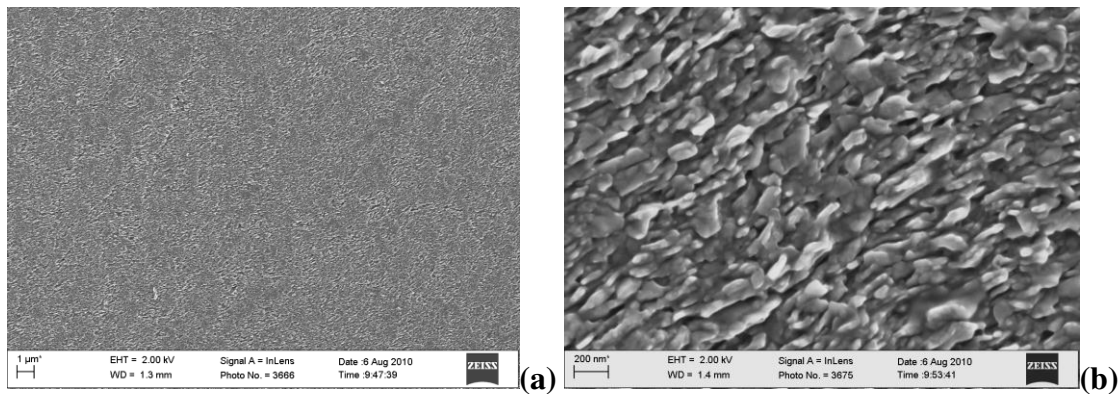

Figure 6-5:   *SEM images for PyC annealed at 1000 °C for 9 hours. (a) Lower magnification with the size bar = 1 µm. (b) Higher magnification with the size bar = 200 nm.*
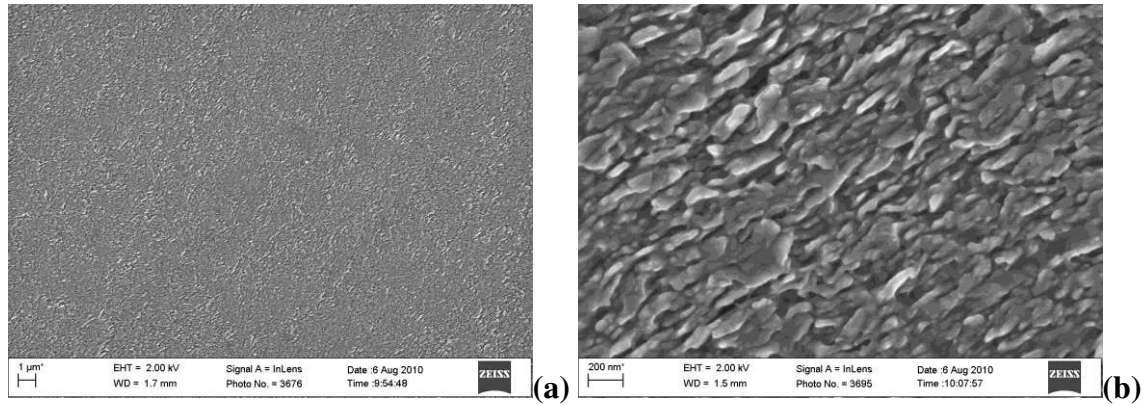
Figure 6-6: *SEM images for PyC annealed at 1100 °C for 9 hours. (a) Lower magnification with the size bar = 1 μm. (b) Higher magnification with the size bar = 200 nm.*

Figure 6-7: *SEM images for PyC annealed at 1200 °C for 9 hours. (a) Lower magnification with the size bar = 1 μm. (b) Higher magnification with the size bar = 200 nm.*
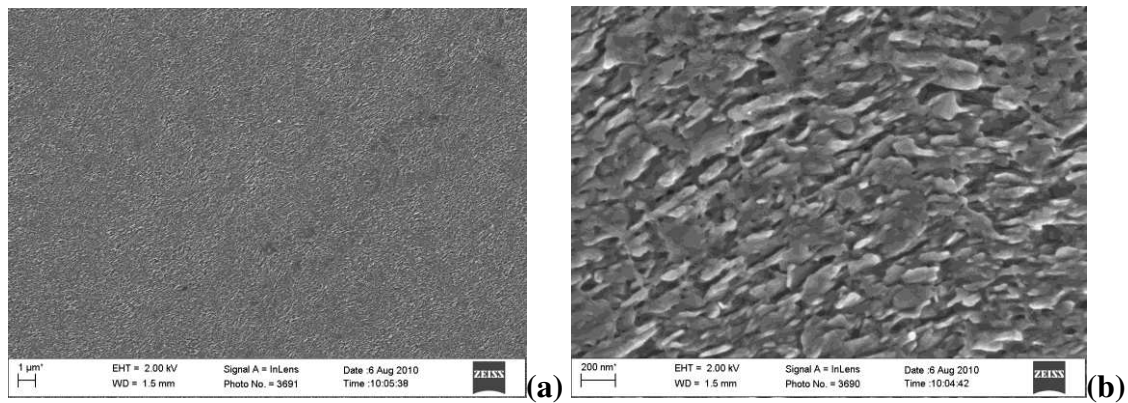
From the above it follows that the SEM results have so far helped to identify the structure of the PyC used in this study. SEM showed that sample preparation can lead to crack formation which could detrimentally affect our other experimental results. By comparing our images with ones reported in the literature we could conclude that our samples contain graphitic layers with medium to high degree of preferred orientation and may be classified as laminar. SEM also showed that the surface microstructure of the samples changed with increasing annealing temperature.

6.2 XRD RESULTS

The following XRD results will show and discuss the relationship between the degree of preferred orientation and heat treatment of PyC. This will later be compared with the behaviour of iodine after heat treatment in order to establish how preferred orientation affects iodine behaviour.

As discussed in section 4.3.1, the degree of preferred orientation of the graphitic layers in the PyC is directly proportional to the intensity of the $C_{(002)}$ peak obtained in XRD. The aim of the following XRD results was to demonstrate the above and compare it with the results obtained from the RBS depth profiles, which will be discussed in section 6.3.

The XRD results were obtained from the samples with the X-ray beam incident on the surface parallel to the graphitic layers, as shown Figure 6.8.
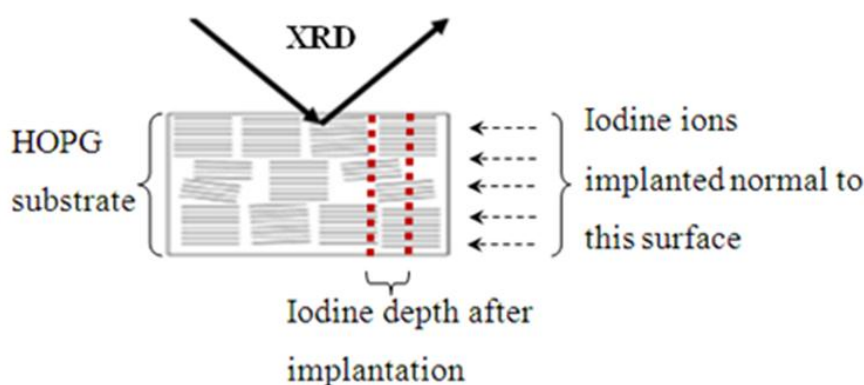

Figure 6-8: *Schematic diagram illustrating the PyC surface used for ion implantation of iodine and the surface used for XRD measurements.*

In Figures 6-9 and 6-10, the XRD results obtained from the samples before annealing (as-implanted) and after annealing at 1000 °C, 1100 °C, and 1200 °C show that higher annealing temperature results in higher intensity of $C_{(002)}$ peaks; which according to literature [3] implies an increase in degree of preferred orientation of the graphitic layers. The paper by Guellali *et al.* [1], discussed in the previous section, also confirms this. Their XRD results of heat treated PyC resulted in an increase in preferred orientation and the PyC approached the structure of perfect graphite.

The interlayer spacing between the graphitic layers decreased and the crystallite size L_c increased. This behaviour was illustrated using Figure 6-11. This figure shows that heat treatment of both LT-PyC and HT-PyC result in an increase in the degree of preferred orientation of the graphite layers. The correlation between the height of the $C_{(002)}$ peak and the size of the PyC crystallites was also pointed by Li *et al.* [4] in his results reproduced in Figure 4-11.
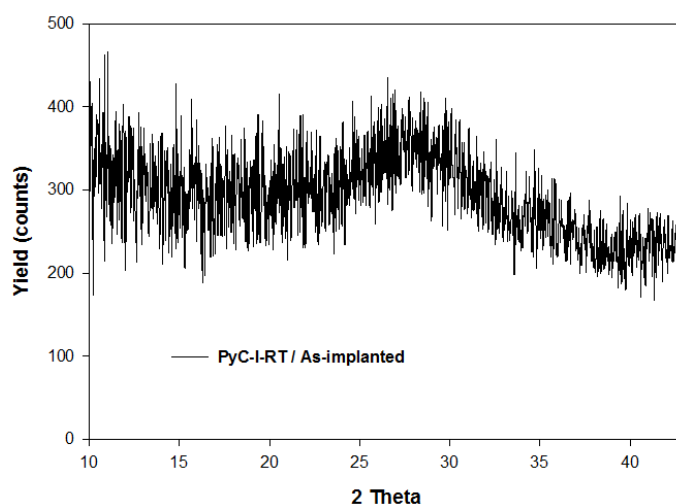

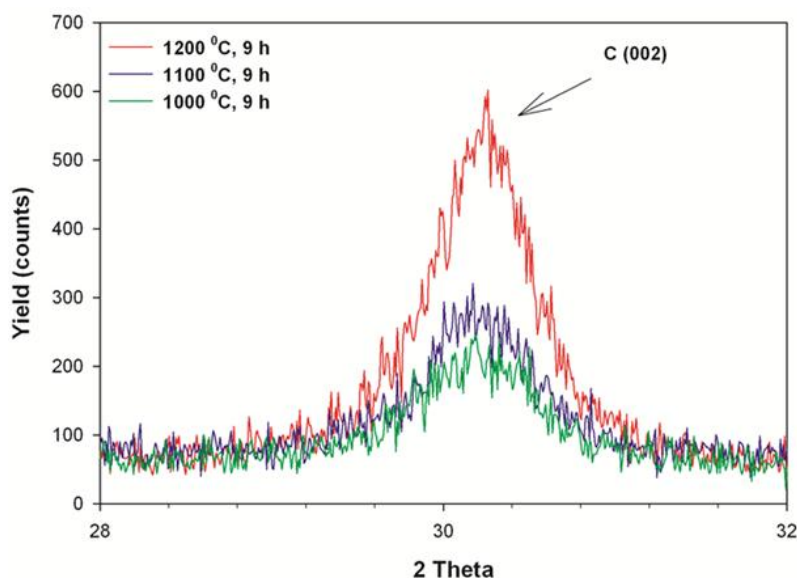**Figure 6-9:**   *XRD scan showing the $C_{(002)}$ peak intensity obtained from as-implanted PyC.*

Figure 6-10:   *XRD scans comparing the $C_{(002)}$ peak intensities obtained from PyC annealed at 1000 °C, 1100 °C, and 1200 °C; all for 9 hours.*
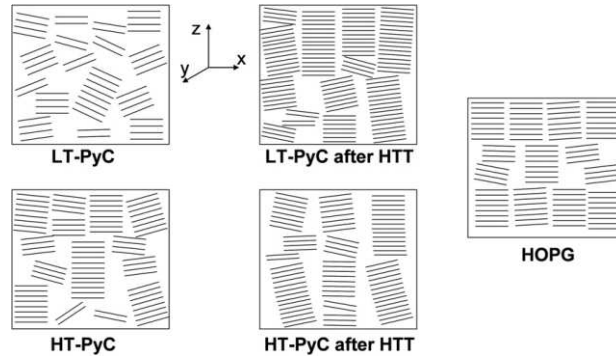
Figure 6-11: *Microstructure of the investigated samples as concluded from the results of the XRD investigations by Guellali et al. [1]. LT-PyC = PyC deposited at low temperature; HT-PyC = PyC deposited at high temperature.*

Our XRD and SEM agree with the above studies [4]. Our SEM results presented in Section 6.1 showed a growth in the crystallite size with increasing annealing temperature which in turn led to an increase in the corresponding increase in the $C_{(002)}$ peak.

6.3   RBS RESULTS

SEM and XRD revealed more details about the PyC behaviour than about the iodine behaviour after heat treatment. The following RBS results show and discuss the behaviour of iodine before and after heat treatment by studying the obtained depth profiles.
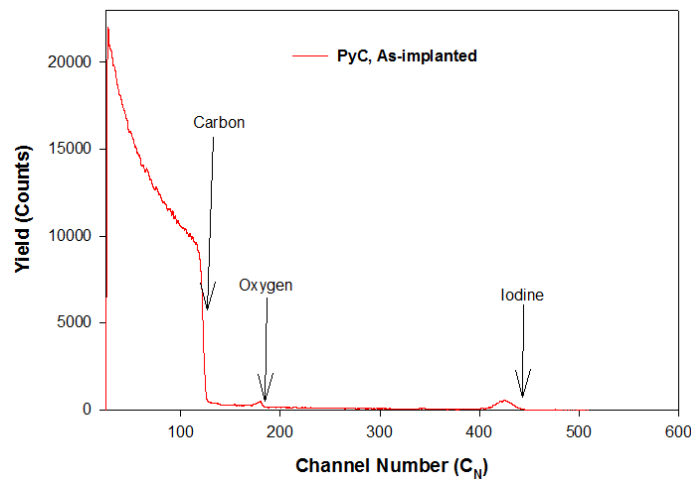

Figure 6-12: *A typical spectrum for the PyC samples used in this experiment. The surface position for carbon is at $C_N = 125$ and the maximum peak height for iodine at $C_N = 424$.*

Figure 6-12 shows a typical spectrum for an as-implanted PyC sample used in this experiment. The surface position for carbon is approximately at channel number, $C_N = 125$. The position of the highest point of the iodine peak (which is approximately equal to the projected range of the implanted iodine ions) is at $C_N = 424$. The full iodine peak ranges from $C_N = 380$ to $C_N = 450$, corresponding to the depth at which iodine ions were implanted into the PyC. An oxygen peak appeared in all obtained PyC spectra, at approximately $C_N = 180$. It is currently not clear why the oxygen appears in all the PyC spectra measured using RBS.
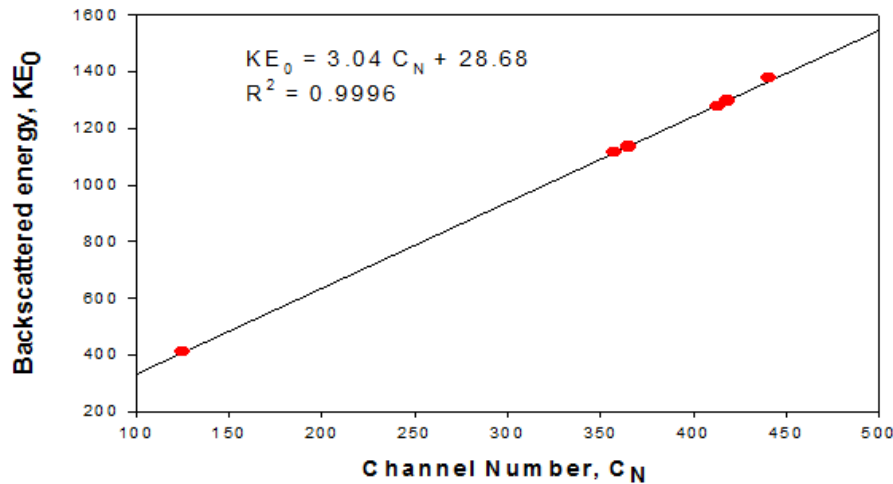

Figure 6-13: *A calibration plot for estimating the surface position for carbon and depth profile for iodine implanted in PyC. The elements used in the calibration samples are given in Table 6-1.*

Table 6-1: *Elements and conditions used to create a surface position calibration plot (Figure 6-13). The kinematic factors, backscattered energy and channel numbers for the elements are also shown.*

Element	Kinematic factor, K	Backscattered energy, $E_0 K$	Channel Number, C_N	Incident Energy, E_0 (MeV)
Pd	0.8624	1380	441.0	1.600
C	0.2559	409.4	125.0	1.600
Ga	0.7977	1276	413.5	1.600
As	0.8104	1297	419.0	1.600
Ga	0.7977	1117	357.5	1.400
As	0.8104	1135	365.0	1.400

The energy calibration (keV/channel) was converted to a depth calibration (nm/channel) using the computer program STOP2 [5]. This program uses energy loss data in Ziegler *et al* [6].

In order to validate the obtained PyC spectra, the measurement results were compared with the results obtained using the transport of ions in matter (TRIM 2008) simulation software program [6]. The TRIM program was used to predict the projected ranges, Skewness, kurtosis and straggling of the implanted iodine in PyC before and after annealing. As shown in Figure 6-14, the skewness tells whether the peak is skewed towards the surface (negative values) or away from the surface (positive values). So, it can be concluded from the skewness data in Figure 6-13 that the iodine peak (as-implanted) from the measured results is skewed deeper into the PyC than the simulated results.
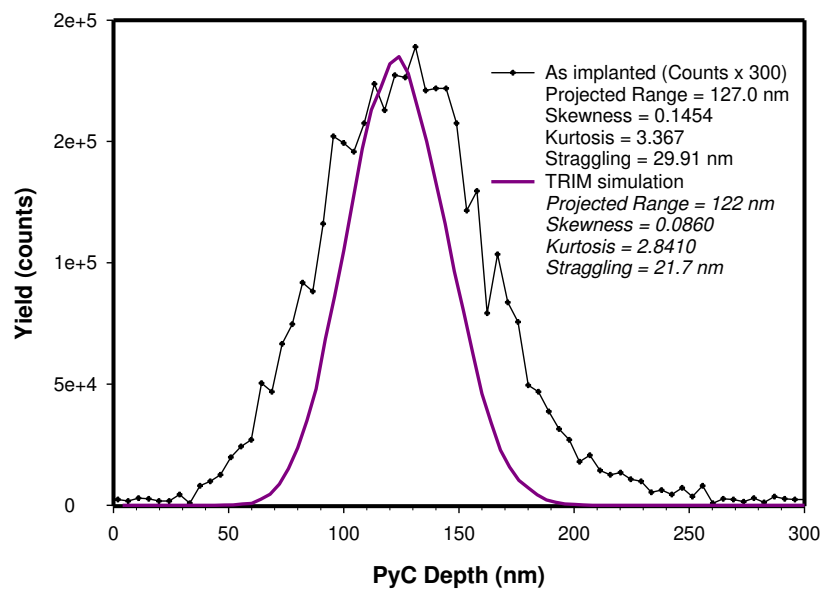

Figure 6-14: *A comparison of the iodine peak obtained from measurement of the as-implanted samples with that obtained from TRIM simulation. The counts from the as-implanted peak were all multiplied by 300 for easy comparison.*

Kurtosis indicates the extent of the distribution tails, with a value of 3.0 indicating a Gaussian distribution. In general, values from 0 to 3 indicate abbreviated tails, and values above 3.0 indicate broad tails. The distance travelled by the iodine ions from the surface of the PyC to the point where the ion energies fall to below 20 eV and cease to move is referred to as total range. Therefore, the projected range, R_p, is the range obtained when the range is measured parallel to the incident ion direction. Range straggling has already been discussed in chapter 4. The TRIM program is capable of achieving a moderate degree of accuracy with approximately 5 to 10 % error.

The disagreement in the projected range, Skewness, kurtosis, and straggling when comparing the experimental with the TRIM results, as shown in Figure 6-14, is due to the following reasons. TRIM does not take into account the crystal structure of the PyC and its structural defects. Consequently, it ignores any channeling of the bombarding ions. It also does not take into account the fact that iodine ions may cause structural damages on the PyC during implantation as well as the channeling of bombarding ions. Additionally, TRIM's predictions of the projected ranges are based on binary collisions, i.e. the influence of neighboring atoms is neglected. The recombination of interstitials with vacancies is neglected. The electronic stopping power is an averaging fit from a large number of experiments. The target atom which reaches the surface can be sputtered if it has enough momentum and energy to pass the surface barrier. It assumes a layered system, i.e. simulation of materials with composition differences in 2D and 3D is not possible [7].
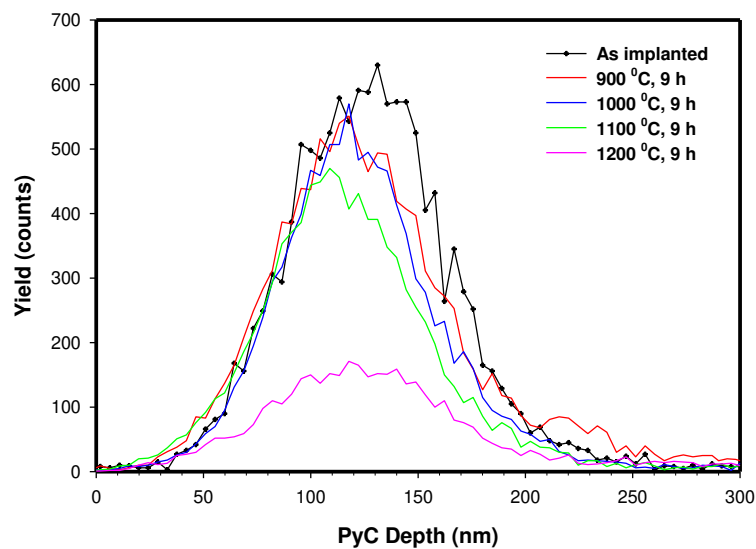

Figure 6-15: *RBS spectra of the implanted iodine is compared before and after annealing at 900 °C, 1000 °C, 1100 °C, and 1200 °C. The iodine was implanted at room temperature at energy of 360 keV.*

The RBS depth profiles of the implanted iodine distributions before and after annealing are shown in Figure 6-15. Three features are particularly obvious from a cursory glance at the data. The peak heights decreased with increasing annealing temperature indicating a loss of iodine from the iodine profile as detected by RBS. The peak positions also changed with annealing temperature. Lastly, there was significant scatter in the data which was also attested by fitting of the data. The fitting to each dataset was done using the computer

software program, Genplot [8]. The first two moments (i.e. the projected range and the range straggling with the latter to the FWHM of the peak) to a Gaussian type distribution were determined from the fit.

To ensure thorough analysis of the results, the FWHM were determined by first fitting the whole distribution of data. Secondly, fitting was performed on the distribution along the implanted region ranging from 0 nm to the depth just beyond the maximum peak height or projected range; hereafter called the front side fit. Lastly, fitting was also performed on the data from the depth just before the maximum peak height to the end of the peak which is deeper into the bulk; hereafter called the bulk side fit. In the latter two cases one to three data points before or beyond the maximum peak position were chosen. In principle, these three different fits could provide evidence on whether diffusion of the implanted iodine took place and whether there was a preferred diffusion direction, i.e. towards the surface or towards the bulk of the PyC. The projected range and FWHM results are shown in Table 6-2; and Figure 6-16 is a graphical representation of the projected ranges shown in Table 6-2; while Figure 6-17 shows the FWHM versus annealing temperature.

Table 6-2:   *Evaluation results for the PyC samples; they were evaluated using the Gaussian non-linear square fitting method. The "error" designates a statistical error as calculated by the Genplot program.*

PyC Sample	Projected Range (R_p) (nm) [Error]	FWHM (Full Peak) (nm) [Error]	FWHM (Front Side) (nm) [Error]	FWHM (Bulk Side) (nm) [Error]
As-Implanted	125.6 [0.5]	81.01 [1.4]	84.07 [4.5]	78.18 [2.8]
900 °C	119.4 [0.6]	83.36 [1.6]	84.54 [2.8]	92.54 [4.9]
1000 °C	118.0 [0.4]	76.77 [1.2]	72.99 [2.1]	85.24 [2.8]
1100 °C	113.2 [0.4]	79.12 [1.2]	72.23 [2.6]	92.31 [2.8]
1200 °C	121.6 [0.6]	89.48 [1.9]	99.61 [5.7]	82.89 [2.8]

Figure 6-16 shows an overall decrease in the projected range (R_p) values between as-implanted and 1100 °C annealing temperature sample. The corresponding iodine profiles look asymmetric, i.e. broader on the side (i.e. the bulk side) deeper into the PyC bulk than the side towards the surface (i.e. the front side). This suggest that, between 900 °C to 1100 °C, there was more transfer of iodine deeper into the PyC bulk than towards the PyC surface.
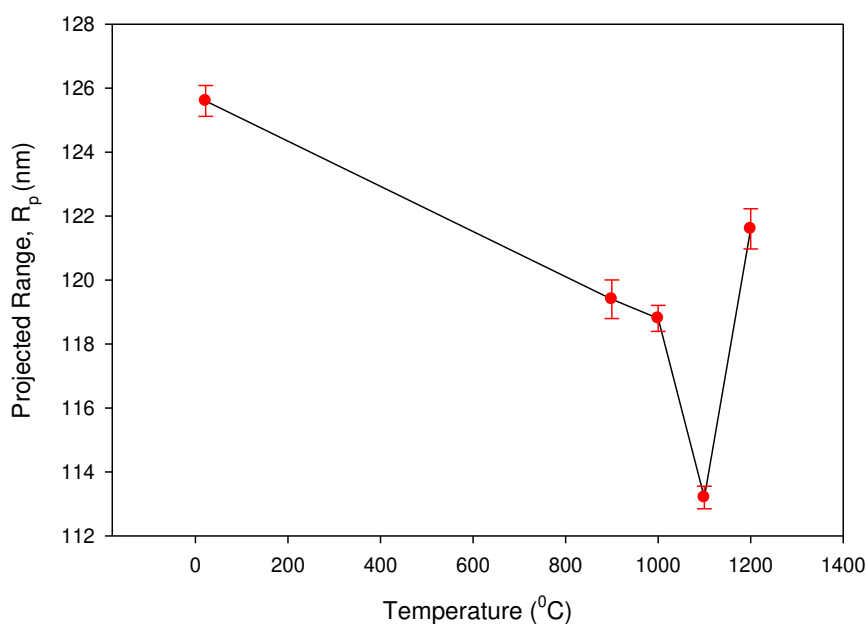

Figure 6-16:   *Change in projected range (R_p) with annealing temperature (900 °C, 1000 °C, 1100 °C, and 1200 °C).*

In contrast, annealing at 1200 °C caused the projected range value to increase again and the peak shape became more symmetric than the peaks obtained between 900 °C and 1100 °C. So, more iodine was transferred towards the PyC surface at 1200 °C than during the 900 to 1100 °C annealing temperatures. In the un-implanted region where most, if not all, the carbon atoms were still in their original positions, the implanted iodine might still move freely through the channels between the graphitic layers. As discussed in section 4.2.2, ion implantation causes structural defects in the PyC, reduces the degree of preferred orientation of the graphitic layers in the PyC and might cause the PyC to become amorphous (or to damage the PyC) in the implanted region. This might reduce the free movement of iodine towards the PyC surface (implanted region) between 900 and 1100 °C annealing temperatures. Again, as discussed in section 4.2.2, high temperature treatment repairs the damaged region in the PyC. After annealing the PyC at 1200 °C, damages caused by ion implantation might become repaired; the degree of preferred orientation increases and the

PyC returns close to its original structure. This will cause the iodine to move more freely through the channels between the graphitic layers. Therefore, structural damage caused by ion implantation plays a major role in the behaviour of iodine in PyC.

From Figure 6-15 it is evident that the area under all the annealed iodine distributions decreased with increasing isochronal annealing temperatures. This means that iodine has both diffused deeper into bulk reaching concentrations below the detection limit for RBS and diffused to the surface where it escaped into vacuum via sublimation. As will be discussed later in this section, the shapes of the distribution suggest the latter mechanism.

In Figure 6-17, the FWHMs obtained by fitting the full iodine distributions, i.e. from 0 nm to the end of the peak at around 250 nm, are indicated by the red data points. As discussed above, the transfer of iodine deeper into the PyC bulk is different to the transfer towards the PyC surface, resulting in asymmetric peaks. As was mentioned above, the FWHMs were also evaluated by fitting a Gaussian distribution to the front sides and the bulk sides of the different iodine profiles.
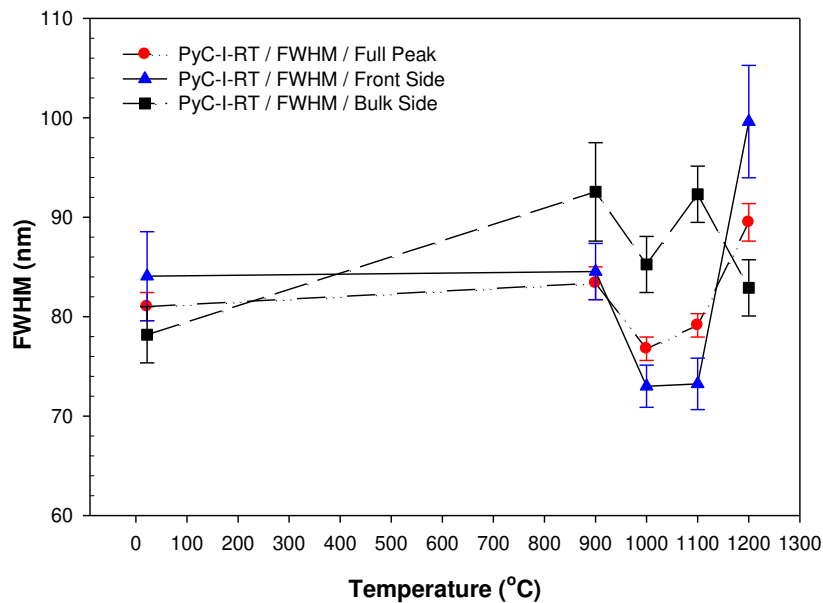

Figure 6-17: *Graphical representation for the change in full width at half maximum (FWHM) of the iodine profiles with annealing temperature (900 °C, 1000 °C, 1100 °C, and 1200 °C).*

As was discussed in section 2.2, a broadening of the implanted iodine profile after annealing is linked with Fickian diffusion. However, from Figure 6-17 it follows that there is no clear evidence of a broadening of the full profile. Thus, the iodine loss at increasing annealing temperatures does not appear to have occurred by means of Fickian diffusion mechanism. The iodine profile annealed at 1200 °C did show broadening of the peak compared to the as-implanted profile. However, the significant loss of iodine resulted in small peaks, which together with the scatter in the data preclude us making definite predictions. Better data and more measurements at annealing temperatures below and above 1200 °C, coupled with isothermal annealing profile measurements are needed to make such predictions.

Separate Gaussian fittings to the front and bulk sides of the profile did not provide clear evidence of a Fickian diffusion mechanism for the implanted iodine after annealing. Fitting the sample bulk side of the iodine profile (cf. the black squares in Figure 6-16) indicated broadening only after annealing at 900 °C. Thereafter, it did not show any broadening of the profile. The surface side of the peak (cf. the blue triangles in Figure 6-16) also did not clearly indicate a broadening of the peak with increasing isochronal annealing temperature, except at 1200 °C annealing temperature.

If we assume that Fickian diffusion occurred, for example, towards the PyC bulk, the diffusion parameters for such diffusion can be determined using the equations 2-14 and 2-15. Substituting the FWHM values at the temperatures 900 °C, 1000 °C, 1100 °C, and 1200 °C in the fourth column of Table 6-2 into the following equation, $D = \dfrac{[W(t)]^2 - [W(0)]^2}{4t\ln(2)}$, the diffusion results shown in Figure 6-18 were obtained.

The data shown in Figure 6-18 confirms the previous conclusion that more data and better data points are needed. Hence, the activation energy, E, and the pre-exponential factor, D_0, could not be determined by fitting the Arrhenius equation, to the data in Figure 6-18. The data is too unreliable to make any real conclusions. The extra measurements as pointed are presently underway.
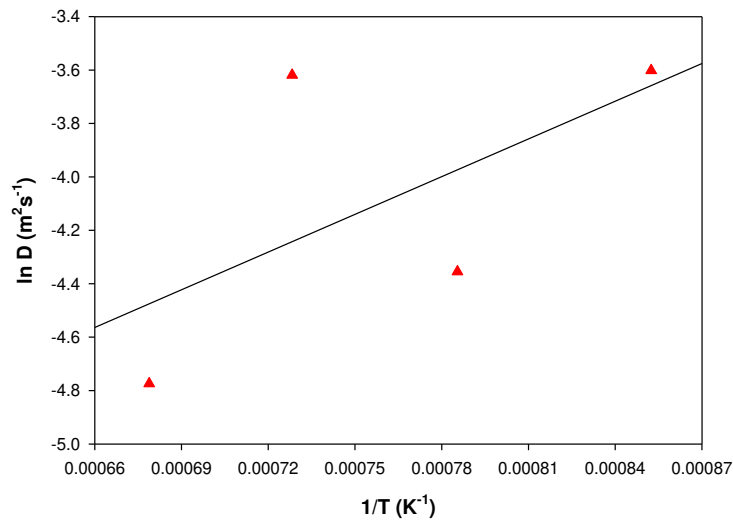
Figure 6-18: *Iodine diffusion results after assuming that Fickian diffusion mechanism causes movement into the PyC bulk after annealing at 900 °C, 1000 °C, 1100 °C, and 1200 °C. The data is too unreliable to make any real conclusions.*

The area under each iodine curve in Figure 6-15 is related to the amount of iodine as detected by RBS in the PyC. There was clearly a loss of iodine occurring after annealing. The loss of iodine as a function of annealing temperature is plotted in Figure 6-19.

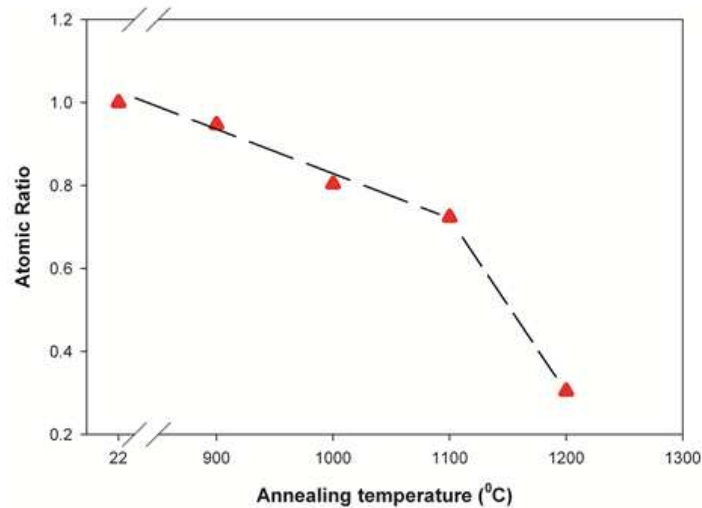**Figure 6-19:** *Comparison of number of iodine ions associated with each peak before and after annealing at 900 ℃, 1000 ℃, 1100 ℃ and 1200 ℃; all for 9 hours. The atomic ratio is the ratio of the number of atoms after annealing to that before annealing.*

The iodine can be lost from the implanted region in the following two ways;

1. Diffusion / segregation to the surface of the PyC where the high annealing temperature would lead to immediate sublimation (at 113.6 °C the heat of sublimation is 7.25 kcal / mol. [9]).

2. Diffusion into the bulk of the PyC with concentrations below the detection limit of RBS.

The iodine loss correlates with what was observed from XRD results in section 6.2 (Figure 6-10). The $C_{(002)}$ peak intensity increased with increasing annealing temperature. This implies that the degree of preferred orientation of the graphitic layers increased with increasing annealing temperature. The spacing between the graphitic layers can act as an easy diffusion plane for the implanted iodine. Therefore, the degree of preferred orientation of the graphitic layers, together with radiation damage, plays major roles in the diffusion behaviour of iodine in PyC.

6.4   REFERENCES

[1]   M. Guellali, R. Oberacker and M.J. Hoffmann. Comp. Sci. and Tech. **68** (2008) 1122-1130.

[2]   J.C. Bokros and R.J. Price. Carbon **3** (1966) 503-519.

[3]   P.L. Walker. Chemistry and Physics of carbon, A series of advances. **5** Marcel Dekker, Inc, New York (1969).

[4]   Z.Q. Li, C.J. Lu, Z.P. Xia, Y. Zhou, Z. Luo. Carbon **45** (2007) 1686-1695.

[5]   E. Friedland, STOP2, Private Communication, Department of Physics, University of Pretoria, (2006).

[6]   J.F. Ziegler, J.P. Biersack and Y. Littmark. The stopping and range of ions in solids, Pergamon Press, New York (1985).

[7]   T.T. Hlatshwayo. Diffusion of Ag in 6H-SiC, PhD thesis, University of Pretoria (2010).

[8]   http://www.genplot.com, 8 July 2010.

[9]   A.J. Moses, The Practicing Scientists Handbook, Van Nostrand Reinhold, New York, (1978) 621.

CHAPTER 7: **CONCLUSSION AND FUTURE WORK**

7.1 CONCLUSION

In this study, iodine ions were implanted into PyC at room temperature. The PyC was annealed at 900 °C, 1000 °C, 1100 °C and 1200 °C. SEM and XRD were used to study the structure of the PyC before and after annealing at the above temperatures. RBS was used to produce profiles of the implanted iodine before and after all the above annealing temperatures. These profiles were used to study the behavior or diffusion of iodine in PyC after heat treatment. The results obtained using RBS were compared with the results obtained using XRD and SEM, leading to the following conclusions.

SEM and XRD studies have revealed the role that the structure of the PyC plays on the behavior of the implanted iodine. Using SEM and comparing with literature, the structure of the PyC used is very similar or close to the laminar structures. Isotropic PyCs are used in the design of TRISO particles. The graphitic layers in the PyC have medium to high degree of preferred orientation. The degree of preferred orientation of the graphitic layers in PyC increased with increasing annealing temperature, as shown by our XRD measurements, in line with reports in the literature.

Our PyC samples have failed to contain the implanted iodine from the first annealing temperature. By studying the projected ranges of the iodine profile before and after heat treatment, it can be concluded that the PyC damage due to iodine implantation reduced or delayed the overall diffusion of iodine towards the surface. According to our XRD measurements, at least some of the damage was annealed out after annealing at 1200 °C. For those samples, the diffusion of iodine towards the PyC surface increased. The evaluation of the FWHM showed that the implanted iodine did not behave the same way when diffusing deeper towards the PyC bulk and when diffusing towards the surface. Iodine diffusion in both directions could not be attributed to Fickian diffusion because there was no clear evidence of the broadening of the iodine profiles using the measured data.

In general, the diffusion of iodine in PyC occurred simultaneously towards the surface of the PyC where the high temperature led to immediate sublimation from the surface; and deeper

towards the PyC bulk with concentrations below the detection limit of RBS. Because of the damage on the PyC due to ion implantation, more iodine is initially transferred deeper into the PyC bulk than towards the PyC surface. After annealing at 1200 °C, the iodine transfer towards the surface increased.

7.2   FUTURE WORK

More work must be done in order to gain more insight on how the PyC structure influences the behaviour of the implanted iodine. Further investigations will be performed using both SEM and XRD, where for instance the Scherrer equation will be used to monitor the crystallite sizes of the PyC before and after heat treatment. Raman spectrometry will also be employed where the sp^2 and sp^3 bonding will be monitored to study the PyC structure before and after implantation and heat treatment.

It has already been explained that iodine implantation causes structural damages on the PyC and that this affects the behaviour of the implanted iodine. In future, iodine will be implanted into the PyC at higher temperature to minimize these damages. Thereafter, the diffusion of iodine will be investigated.

To improve the results, more data for iodine profiles must be collected and short interval isochronal and isothermal annealing must be performed. Higher fluence / ion dose during ion implantation of iodine will be used to improve the sensitivity on the iodine profiles.

Since some implanted iodine diffuses deeper into the PyC substrate, future work may employ secondary ion mass spectrometry (SIMS) to investigate the behaviour of iodine as it moves deeper into the PyC bulk. SIMS is known to have better detection limits for implanted species than RBS.

Other materials such as glassy carbon and isotropic pyrolytic carbon will be investigated after iodine is implanted into these materials. Glassy carbon is reported to be more stable and has a much less preferred orientation of the graphitic layers than the PyC used in this study. Isotropic carbon also has graphitic layers with less degree of preferred orientation compared to the PyC used in this study.